ULTRA-NEAR-SURFACE GALLIUM-ACTIVATED 435NM

LUMINESCENCE FROM DONOR-ACCEPTOR-PAIR

RECOMBINATION IN ION-BEAM IMPLANTED 4H SIC

BY

ZHIMIN GAO, B.Eng.

A THESIS SUBMITTED TO THE DEPARTMENT OF MATERIALS SCIENCE AND

ENGINEERING AND THE SCHOOL OF GRADUATE STUDIES OF

MCMASTER UNIVERSITY

IN PARTIAL FULFILMENT OF THE REQUIREMENTS FOR THE DEGREE OF

MASTER OF APPLIED SCIENCE

Master of Applied Science (2025)   McMaster University

Department of Materials Science and Engineering   Hamilton, Ontario, Canada

TITLE: Ultra-near-surface gallium-activated 435nm luminescence from donor-acceptor-pair recombination in ion-beam implanted 4H SiC

AUTHOR: ZHIMIN GAO

B.Eng. (Materials Science and Engineering),

McMaster University, Hamilton, Canada

SUPERVISOR: Professor Adrian Kitai

NUMBER OF PAGES: xi, 76

Abstract

Silicon carbide is the first material to exhibit electroluminescent characteristics and was used in the LED industry due to its ability to emit blue light. Although alternative materials have been developed to address the lower emission efficiency and challenging manufacturing conditions of SiC, the recent demand for rare-earth free phosphor materials has revived interest in DAP SiC as a potential candidate for LED applications. Its high quantum efficiency, better color rendering, sustainability, and cost advantages make it a promising option.

A general introduction to SiC material properties is given in Chapter 1, including developments of SiC crystal growth, luminescence applications and the mechanism of donor-acceptor recombination. Chapter 3 elaborates on the experiments and characterization methodologies used. A brief description of each method, along with a detailed discussion of their advantages and the reason for selection, will be provided.

In this thesis, gallium and nitrogen co-doped 4H-SiC luminescence is achieved through the ion implanting of highly spatially resolved Ga patterns into n-type SiC with the assistance of an ion milling tool. A [0002] oriented AlN thin film is manufactured by using sputtering techniques, and the influence of sputtering parameters on crystal orientation is discussed in Chapter 4. The AlN encapsulation layer serves to protect and passivate the SiC and nano-scale ion implantation regions under extreme annealing conditions.

Chapter 5 presents and analyzes the experimental results, including photoluminescence (PL) and cathodoluminescence (CL), to identify the emission characteristics of the material and

the associated defect energy levels. Surface characteristics of both SiC and AlN thin films are determined using SEM, TEM, and Raman spectroscopy. The morphological evolution of SiC cross-sections annealed at different temperatures is discussed in Chapter 6.

Finally, Chapters 7 and 8 cover the conclusions and prospects of the project.

Acknowledgements

I would like to express my gratitude to all who supported me during my graduate study:

Thank you for your help for me to be able to complete my degree.

Firstly, I would like to express my appreciation to my supervisor, Prof. Adrian Kitai, for the research scientific and financial support during my graduate study. It is a great honor for me to thank my committee member, Prof. Maureen Joel Lagos, who kindly provided academic advice during the study.

It is also a great honor for me to thank:

All staff in CCEM and CEDT helped me to manufacture and characterize my DAP SiC.

Sabaa Rashid, Betty Huang and Carmen Andrei helped me with the TEM samples preparation and TEM characterization section.

Tingwei Zhang, Zimo Ji, and Bawa Salman for sharing valuable insights and helpful discussions.

Table of Contents

List of Figures

List of Tables

List of Acronyms

Simple cubic (SC)

Hexagonal close-packed (HCP)

Physical vapor transport growth (PVT)

Light emitting diode (LED)

Metalorganic chemical vapor deposition (MOCVD)

Double-heterojunction (DH)

Cerium-doped yttrium-aluminum garnet phosphor (YAG: Ce)

Focused Ion Bean (FIB)

Silicon Carbide (SiC)

Aluminum Nitride (AlN)

Gallium phosphide (GaP)

Gallium Nitride (GaN)

Donor Acceptor Pair (DAP)

Ionized water (DIW)

Photoluminescence (PL)

Cathodoluminescence (CL)

Quattro environmental scanning electron microscope (ESEM)

Transmission Electron Microscopy (HRTEM)

Energy Dispersive X-Ray Analysis (EDX)

X-ray diffraction (XRD)

Longitudinal optical phonon plasmon coupled (LOPC)

Transport of Ions in Matter (TRIM) and SRIM (Stopping and Range of Ions in Matter)

1 Chapter 1: Introduction to Silicon Carbide

1.1 General Introduction to Silicon Carbide

As a compound semiconductor material, silicon carbide (SiC) has one of the strongest covalent bond strengths between silicon and carbon, which allows SiC to have widespread use in power electronics applications. Compared to conventional semiconductors such as silicon, the outstanding physical and electronic properties of SiC make it an irreplaceable choice due to its excellent stability[1]. The formation of a native oxide layer via the thermal oxidation method provides SiC with great compatibility with Si manufacturing techniques. Additionally, the wide doping range for both n and p-type dopants offers SiC a unique advantage for commercialization among a series of wide bandgap materials such as GaN, C(diamond), and gallium oxide[2, 3].

The relatively large effective electron mass in SiC is attributed to a smaller reciprocal lattice parameter, which results in a smaller electron mobility in SiC. Nevertheless, the high breakdown field and electron saturation velocity of SiC devices have enabled operation at higher frequencies. Furthermore, the high breakdown field allows SiC devices to operate with voltage-blocking layers that are ten times thinner while having doping concentration 2-3 orders of magnitude higher, which results in lower on-state resistance compared to the Si counterpart devices[4].

The wide band gap nature of SiC makes it a promising material for high-temperature applications due to its low intrinsic carrier concentrations. Moreover, the wide band gap

nature of silicon carbide enables a wide range of visible wavelength light emission corresponding to the different bandgap energies of the SiC polytypes[5-7].

1.2 Silicon carbide polytypes

As a compound wide band gap semiconductor material, silicon carbide is well known for its polytypism, with over 250 polytypes in nature. [8]. Among these polytypes, 3C-SiC, 4H-SiC, and 6H-SiC are the most commercially successful in the fields of power electronics and LED applications.
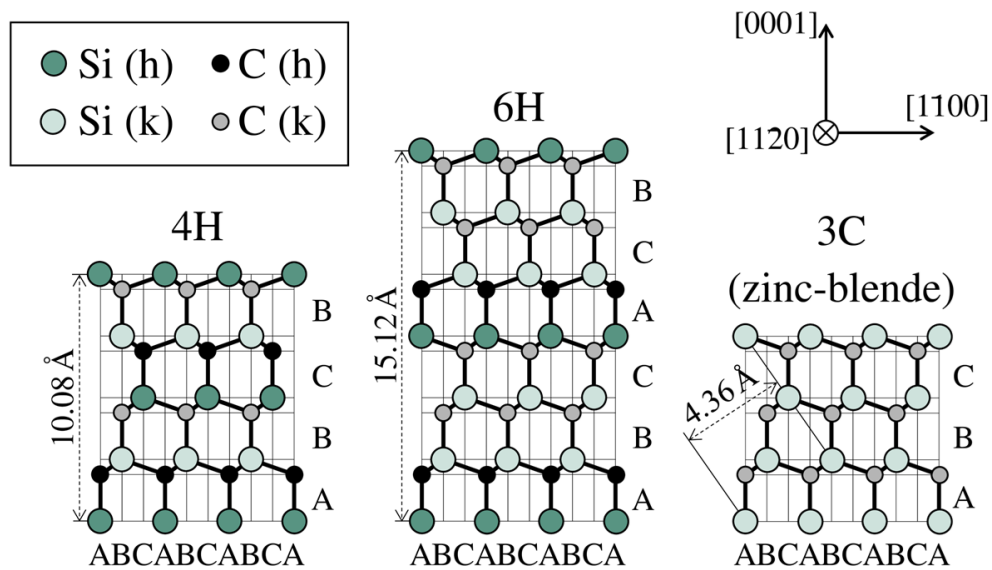
Figure 1.1 SiC Polytypes 4H, 6H and 3C[9]

The major differences between the polytypes are the stacking sequence of silicon carbide bilayers as well as the crystal structures. Among the three most commercially available polytypes, 3C-SiC is the only polytype with a simple cubic (SC) crystal structure, whereas 4H and 6H SiC both have a hexagonal close-packed (HCP) crystal structure. Referring to

Figure 1.1, the stacking sequences of 4H SiC are ABCB and ABC for 3C SiC. For SiC polytypes with hexagonal crystal structures, the stacking sequences generate distinct sublattices in which carbon and silicon atoms can occupy either hexagonal sites or cubic sites[9]. The different sublattice sites can vary the energy level in the band gap due to the potential differences in the lattice structure[10]. Furthermore, SiC also possesses different atomic forces depending on the orientations. The plane with Si dangling bonds on the surface is denoted as the Si face, whereas the Carbon face has a Carbon dangling band on the surface. In 4H-SiC, the Si face plane and the carbon face plane are oriented in (0001) and (000-1) directions, respectively. The types of dangling bonds can decide which ligands or ions can attach to the surface, and the surface characteristics can be influenced mainly by the attached ligands or ions in terms of surface passivation[9, 11].
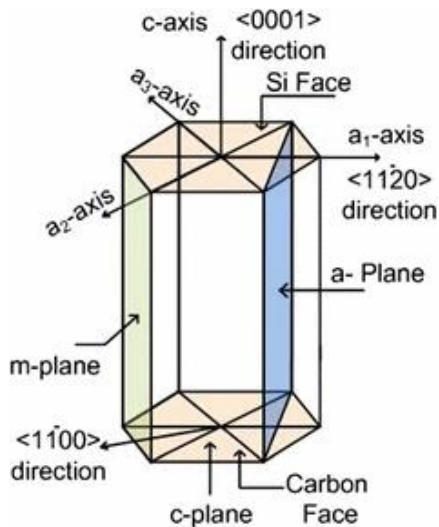
Figure 1.2. 4H SiC crystal structure[12]

1.3　Silicon carbide material and electronic properties

Silicon and carbon are covalently bonded in the form of tetrahedral structures. Due to the distinction in stacking sequences, the periodicity and potential of crystal lattices among different polytypes vary. Thereby, despite that all polytypes share the exact chemical stoichiometry, the properties of each polytype are distinctive.

Properties	4H-SiC	6H-SiC	3C-SiC
Lattice Constant (Å)	a=3.09 c=10.08	a=3.09 c=15.12	4.36
Bandgap (eV)	3.26	3.02	2.36
Breakdown field $N_D = 10^{17} cm^{-3}$ ($MVcm^{-1}$)	∥ $c-axis$: 3 ⊥ $c-axis$: 2.5	∥ $c-axis$: 3.2 ⊥ $c-axis$: > 1	1.8
Hole mobility at $N_A = 10^{16} cm^{-3}$ ($cm^2V^{-1}s^{-1}$)	115	90	40
Electron mobility at $N_D = 10^{16} cm^{-3}$ ($cm^2V^{-1}s^{-1}$)	∥ $c-axis$: 800 ⊥ $c-axis$: 800	∥ $c-axis$: 60 ⊥ $c-axis$: 400	750
Thermal conductivity ($Wcm^{-1}K^{-1}$)	3-5	3-5	3-5
Electron saturation velocity ($10^7 cms^{-1}$)	2	2	2.5
Donor dopants and shallowest ionization energy (meV)	N:45 P:80	N:85 P:80	N:50
Acceptor dopants and shallowest ionization energy (meV)	Al: 200 Ga:350	Al:200 B:300	Al:270

Table 1.1. Comparison of electronic properties of major SiC polytypes at 300K [13, 14].

Table 1.1 Presents the selected electronic properties of three major SiC polytypes. Compared to the hexagonal structure polytypes, the 3C-SiC material exhibits isotropic properties due to its simple cubic structure. The more significant number of stacking bilayers in 6H-SiC compared to 4H-SiC also reflects on the electronic properties. The 6H-SiC c-axis lattice constant is slightly larger than 4H-SiC, resulting in less isotropic electron mobility and breakdown field compared to 4H-SiC[15].

The most iconic feature of SiC is its wide bandgap. Specifically, the bandgap of 4H, 6H, and 3C SiC are 3.26eV, 3.02eV, and 2.36eV, respectively. Owing to the wide bandgap of SiC polytypes, photon emission in the visible wavelength range through band-to-band recombination, corresponding to the wavelength of 380nm, 410nm, and 525nm[14], is possible. The objective of the project is to achieve gallium-nitrogen donor-acceptor pair recombination in 4H-SiC and eventually target this DAP mechanism for a future high-performance white light LED. In order to convert UV emission into blue, green, and red light and then combine to emit white light, a polytype with a bandgap around 3eV is desired. Although 6H-SiC is a more attractive option in terms of bandgap, which perfectly fulfills the requirements, the ionization energy level of impurities in 6H-SiC may limit the light emitting ability of 6H-SiC in the blue light wavelength range. Additionally, 4H-SiC is widely used in the power electronics industry because of its excellent carrier mobility and high break-down field. The lower price of 4H SiC because of its large manufacturing volume is another consideration for the project. Therefore, 4H-SiC was selected in this

project due to its largest bandgap, ability to emit blue light, and relatively lower cost among the three polytypes.

Owing to the bandgap and sublattice energy level difference among the polytypes, the emission wavelength can be used as an indicator to determine the polytypes as well as the ratio of impurities occupying various sublattice sites.[16].

1.4 SiC manufacture

As shown in the SiC phase diagram in Figure 1.3, even with the extreme thermal conditions at 2830℃, SiC can only decompose into C and a Si-solution. The non-uniform and incomplete decomposition of SiC makes crystal growth directly from SiC melt unfeasible[1].
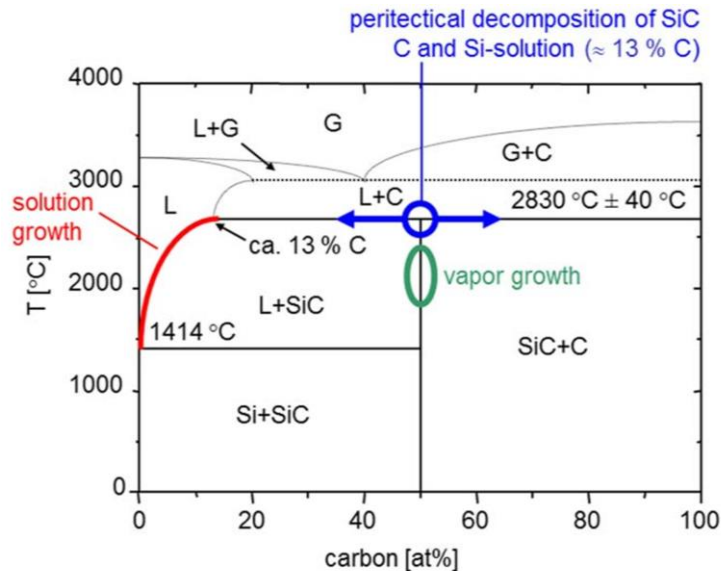
Figure 1.3. SiC phase diagram[1]

The most widely used method for SiC wafer manufacturing in the industry is physical vapor transport growth (PVT), as shown in Figure 1.4. The PVT process was invented by Lely in 1955 and further refined by Tairov and Tsvetkov in 1978[17, 18]. The process involves a series of sublimation and deposition reactions. In this process, high-purity SiC powder is used as a source and heated to 1900-2400°C; the crystal seed is suspended at the top of a crucible; the temperature gradient in the crucible results in a partial pressure difference between the seed and the source, which drives the deposition of SiC crystal. Si, SiC_2 and Si_2C are the three major gas phases that occur during the deposition process. Solid state SiC forms upon the seed through the chemical reaction between Si and SiC_2 gases [18]. Referring to the SiC phase diagram, the solubility of carbon in silicon decreases at temperatures below 2000°C. The application of Si-metal solutions such as Si-Cr, Si-Ti and Si-Al can effectively increase the solubility of C in Si, thereby accelerating the SiC growth rate. However, the use of these metal elements during the growth introduces unintentional doping into SiC crystal, which can potentially change the electronic properties of the crystal[19].
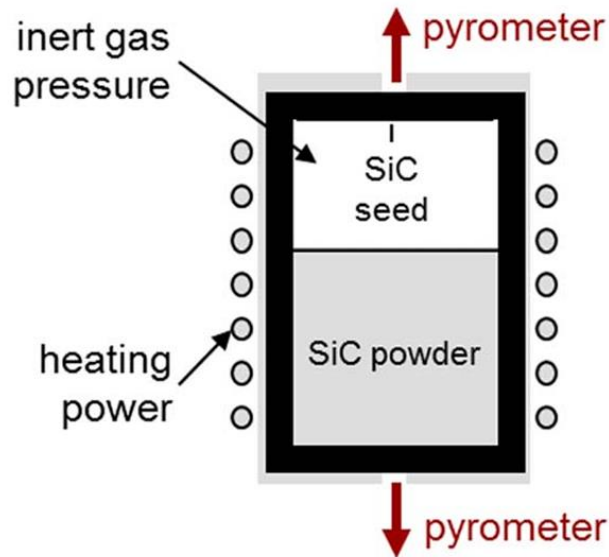
Figure 1.4. The schematic diagram for the SiC physical vapor deposition method[1]

1.5 Light-emitting Diode History

The light emitting diode (LED) as a solid-state light emitting device can effectively emit light via an electroluminescence process[20-22]. The operation of this electroluminescence process relies on the carriers injected under forward bias and recombined in the well-designed p-n junction region[23]. State-of-the-art LED technologies have enabled its dominant position in luminescence and display applications due to its unparalleled luminous efficiency advantage[22]. Additionally, long life span, fast response time, cold light source, and environment-friendly advantages have significantly contributed to the commercial success [22].

Electroluminescence was first observed in 1907 by Henry Joseph Round during his studies with polycrystalline SiC. Later in the 1950s, Infrared LEDs were developed based on GaAs, and then red LEDs were invented based on GaAsP in the 1970s[24]. The GaP-based yellow-green LEDs were developed as the evolution of the industry. Over time, the material of LEDs gradually transfers to the III-V semiconductor and ternary or quaternary compounds. In the 1990s, red, orange, yellow, and green were achieved by implementing AlInGaP material[22].

1.6   Blue LED

Despite the fact that red and green were successfully manufactured in the 1970s, achieving blue LEDs remained challenging until the 1990s due to their shorter emission wavelength[25]. Initially, the research efforts focused on wide bandgap materials such as SiC and II-VI semiconductor ZnSe. However, due to the indirect band gap nature of SiC and the presence of point defects in ZnSe, which result in efficiency and life span problems, the development of SiC and ZnSe-based LED was hampered.

As a wide direct band gap material, GaN showed promising potential for light emission applications. However, the enormous challenges of doping GaN with p-type dopant and growing a high-quality epitaxial layer make the development of GaN-based LED processed slowly.

The issues were solved by introducing novel fabrication equipment using metalorganic chemical vapor deposition (MOCVD). Firstly, the GaN was grown upon an AlN buffer layer deposited on a sapphire substrate. Then, the GaN-Si technique was developed and

inspired by the concepts of an AlN buffer layer to grow GaAs on Si. By growing the GaN buffer layer at lower temperatures, followed by the GaN epitaxial layer at conventional temperatures, a GaN layer with low dislocation density and high uniformity was obtained in 1986[22]. Mg-doped GaN was achieved, but the material did not exhibit a p-type electrical behavior unless the material was electron irradiated. Later research revealed that Mg atoms are passivated by the hydrogen atom from the carrier gas. The thermal annealing was later used to promote the desorption of hydrogen atoms, thereby activating the dopant[22].

A double-heterojunction (DH) structure is essential for high-efficiency LEDs. To achieve DH, the InGaN was used to control the bandgap and lattice constant of the material. However, the lattice constant difference between InN and GaN caused phase separation. In 1989, the issues of phase separation were resolved by carefully controlling the mole fraction during the growth[22].

Finally, in 1994, Japanese company Nichia successfully developed high-brightness blue LED based on InGaN/GaN heterojunction, achieving an external quantum efficiency of 2.2% [22].

1.7 White LED

The realization of GaN-based blue LEDs not only enabled the LEDs to replace conventional illumination technologies but also promoted the development of new display technology such as micro-LED; the versatility of the LED has created a tremendous demand for white light LEDs. There are three approaches for achieving white light LEDs:

multi-chip color mixing, UV LED with phosphor, and blue LED with phosphor[26]. Although the multi-chips color mixing approach offers a high color rendering index, high efficiency, and excellent durability, the emission wavelength and efficiency of the LEDs strongly depend on the operating temperature and current, leading to emission shift. More complex current and temperature control are required to overcome the shifting problems that increase the cost and system complexity[26]. The UV LED with phosphor is a full conversion approach, which usually experiences a significant amount of Stokes shift during the UV down-conversion. In contrast, the blue LED with yellow phosphor approach is the most commercially successful one due to its high efficiency and high power density. Cerium-doped yttrium-aluminum garnet phosphor (YAG: Ce) is selected to partially convert blue light into red and green, combining all three colors to produce white light[26]. With the increasing demand for LED, the price and sustainability of rare earth phosphors drive people to reconsider earth-abundant LED semiconductors such as SiC.

The first commercially available SiC LED was developed by CREE in the mid-1970s; the emission was generated via carrier recombination between donor and acceptor levels [27]. However, due to the indirect bandgap nature of SiC, SiC-based electroluminescent devices exhibit lower efficiency compared to GaN-based LEDs[28, 29]. Despite these limitations, SiC has been shown to perform as a promising down-conversion phosphor material due to its high color rendering and high quantum efficiency[16, 30]. Additionally, as a well-known substrate for nitride-based materials, SiC can potentially serve as both a substrate for GaN and phosphor material simultaneously.

1.8   Research objective

The objective of this research project is to achieve gallium-nitrogen donor-acceptor pair recombination emission in 4H-SiC through ion implantation with the assistance of an ion milling tool (Focused Ion Beam). The high spatial resolution and ultra-shallow ion implanted pattern can potentially be coupled with nitride-based LED for micro-LED display application via a carrier pumping mechanism. As high quantum efficiency and color rendering phosphor material, the vision is to replace expansive rare earth phosphors with DAP-SiC for luminescence and display applications.

2 Chapter 2: Semiconductor background and Donor-Acceptor Recombination mechanisms in SiC

2.1 Band Theory

There are several models that can be used to explain the energy band in semiconductors. The tight binding model is the most widely used. The energy band in a single atom consists of a set of discrete levels for the electrons, electrons can occupy different orbitals and spin states in each energy level. When the atoms are approaching each other in close proximity, the valence electrons have the opportunity to migrate between the atoms due to the overlap of wave function of electrons. Therefore, the extended wave functions of individual atoms combine to form an energy state shared by all valence electrons in the entire crystal. The Pauli exclusion principle dictates that the electrons from the same atomic orbital must occupy a distinct energy state. Hence, in the energy band case, a set of distinct and closely spaced energy states form to accommodate the Pauli exclusion principle. The electron exchange can easily take place among energy states due to the small energy differences of the discrete energy states in the energy band.
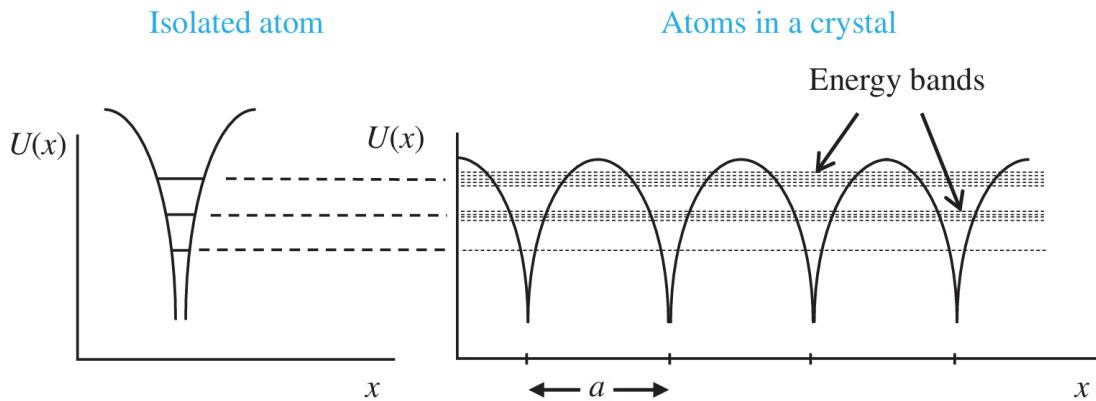
Figure 2.1. Tight binding model of the semiconductor energy band. The single-atom energy level was shown on the left, and the energy level splitting in the crystal was shown on the right[31].

As shown in Figure 2.2, the formation of an energy band in a semiconductor involves orbital hybridization with neighboring atoms. In a Si crystal, the 3s and 3p orbitals hybridize and form a hybridization state with four orbitals. The full and empty orbitals are denoted as bonding and antibonding orbitals, respectively. In the semiconductor material, the bonding and antibonding orbital correspond to the valence and conduction band, respectively; the energy difference between the orbital is defined as the bandgap.
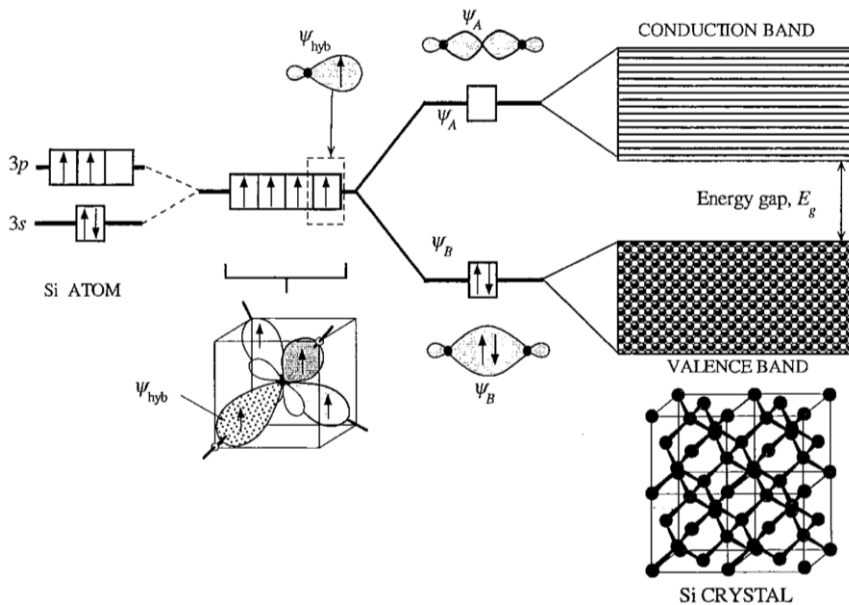
Figure 2.2. The Schematic diagram for the formation of an energy band in Si [32]

2.2 **Direct and indirect bandgap**
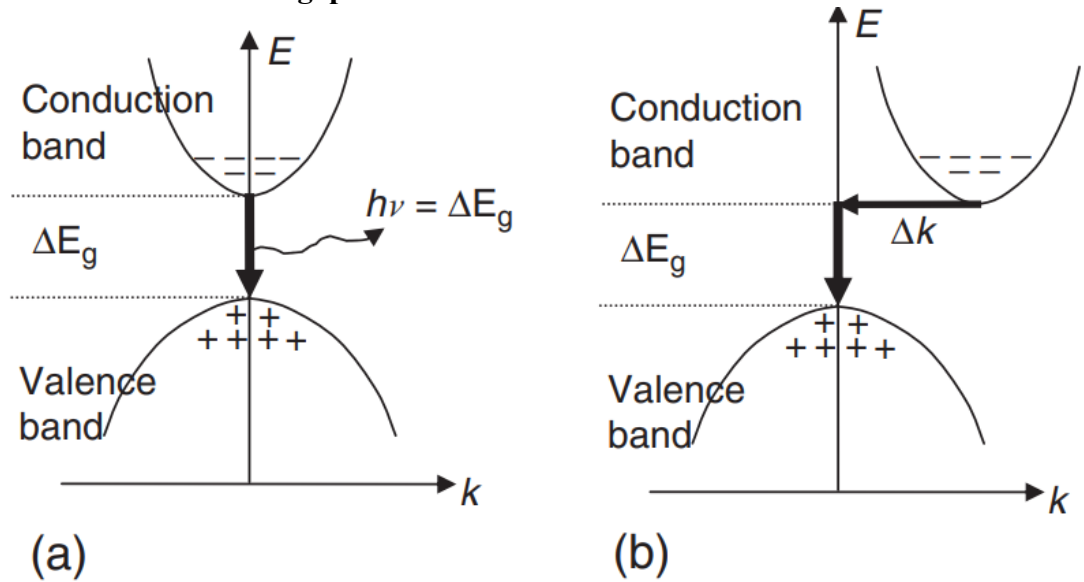
Figure 2.3 shows the simplified schematic diagram of the direct and indirect bandgap recombination process. When the top of the valence band and the bottom of the conduction band share the same momentum value in k-space, the bands are vertically aligned, and the material is defined as a direct bandgap semiconductor material. Oppositely, if the highest energy level in the valence band and the lowest energy level in the conduction band are offset, the material is defined as an indirect bandgap material. The momentum of the lowest energy states in the conduction band is significantly dependent on the lattice structure, which affects both the potential energy and the band structure[31].
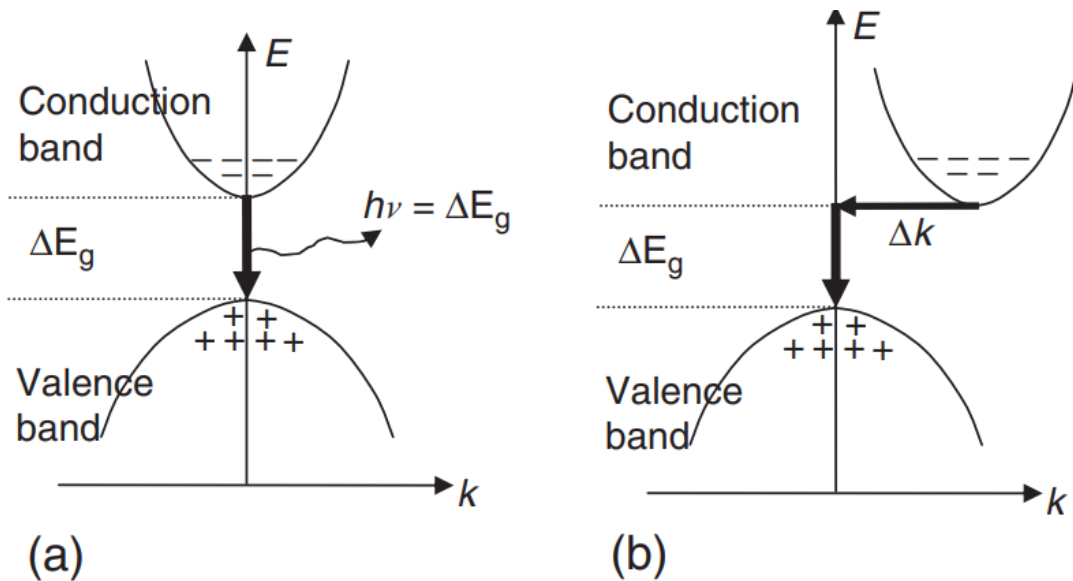
Figure 2.3. Schematic diagram of recombination (a) direct bandgap(b) indirect bandgap[33]

The prerequisite for carrier recombination is the conservation of both energy and momentum. In the direct bandgap scenario, the recombination process and absorption process are completed in a single step, emitting or absorbing a photon with energy equal to the bandgap energy (ΔE_g). Due to the band misalignment in k-space, in most cases, the recombination or the absorption process in the indirect bandgap material typically requires a two-step process with the assistance of a phonon along with a single-step process in which carriers are allowed to migrate directly along the vertical direction from the top of the valence band to higher energy states in the conduction band, unlike conventional band-to-band recombination in indirect material where carriers start at the top of the valence band, and end at the bottom of the conduction band, such a single-step recombination or absorption process requires much larger excitation energy for the carriers[33]. The phonon

16

is a form of lattice vibration that carries tens of millielectronvolts of energy and a large amount of instantaneous momentum. The zero-phonon recombination or absorption in indirect gap material is usually less efficient compared to the phonon-assisted process because of the large energy barrier. As shown in Figure 2.3, while the recombination process is taking place, the momentum from the phonon compensates for the momentum difference Δk of electrons, and then electrons recombine to the valence band and emit photons simultaneously[33]. However, according to the emission spectrum result of 4H-SiC, the most intensive peak related to band-to-band recombination is located around 390nm. Compared to the theoretical 380nm band-to-ban recombination value for 4H-SiC, there is a 10nm shift due to the phonon-involved recombination process, where part of the energy is consumed in the form of phonon energy to overcome the momentum difference. Thus, the efficiency and the rate of recombination in indirect bandgap material is relatively low compared to direct gap material because the involvement of the phonon is less likely to occur within a certain period. Therefore, mainstream luminescence devices are usually made of direct-gap semiconductor materials[31].

2.3 Radiative and non-radiative recombination
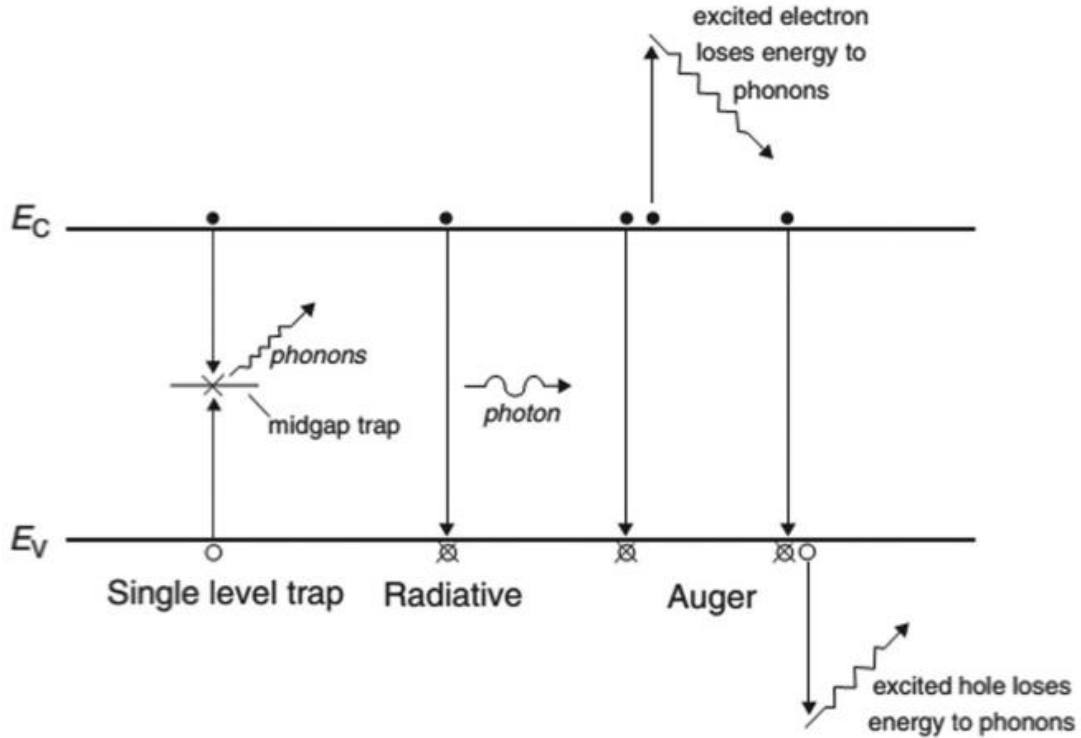
Figure 2.4. Three recombination paths in semiconductor materials[34]

In semiconductors, there are generally three recombination pathways, which can be either radiative or non-radiative. The first type of recombination involves defects in the material. Defects and impurities can act as effective carrier traps. When located in the mid-gap, deep traps can capture either an electron or hole within one diffusion length and become negatively or positively charged. Since these traps have large ionization energy, the trapped carriers will not be easily released. The polarized traps can further attract oppositely charged carriers, promoting carriers to recombine within the traps and emit phonons or

photons. The second pathway is the radiative recombination between conduction band, valence band, and shallow defects[31, 34].

Lastly, Auger recombination is another non-radiative recombination process. The recombination takes place between carriers; one carrier transfers its energy to a neighboring carrier, and the excited carrier migrates to the higher energy level and then releases energy in the form of a phonon and returns to the band edge.

2.4 Donor-Acceptor Pair (DAP)

When a material is simultaneously doped with donors and acceptors, Coulomb interactions take place due to the close proximity between donor and acceptor atoms. When neutral donors and acceptors approach each other, the valence electrons are shared between dopants, which leads to compensation in host materials. The ionization energy of dopants decreases as the electron sharing level increases, which means the dopants are increasingly ionized as the distance between DAP decreases[35].

The recombination energy between donors and acceptors is described by the following equation:

$$E_{pair} = E_g - E_D - E_A + \frac{q^2}{\varepsilon r} \qquad (1)$$

Equation 1. Donor and acceptor recombination energy relationship[35, 36].

Referring to Equation 1, ε represents the dielectric constant of the host material, r denotes as the physical separation between DAP, $E_D \ and \ E_A$ represent the ionization energy of

donor and acceptor, respectively, as isolated impurities. The last term in the equation represents the Coulomb interaction between donors and acceptors in the host material[35].

In order to contribute to the electric properties of the host material, the dopant must be activated either in the form of interstitial diffusion or substitutional diffusion by replacing an atom in the host material matrix. Thereby, in most cases, the physical distance between the donors and acceptors is generally corresponding to the periodicity of the crystal lattice of the host material. As a result, the separation between impurities is a series of discrete numbers that are determined by the distance between the neighboring lattice sites. Additionally, because dopant atoms constitute only a small fraction of the host lattice compared to the number of host atoms, the distribution and separation of impurities are discrete. Based on the last term in Equation *1*, Coulomb interaction intensity is inversely proportional to the separation between the impurities. For the very distance pair, the interaction is negligible, whereas, for the closely spaced situation, the contribution of coulomb interaction can be very pronounced; the energy level of impurity can even shift into the band edge[35].

As mentioned previously, the physical separation of impurities is strongly dependent on crystal periodicity and lattice structure. In the compound semiconductor material, the cation and anions form different sublattices. Additionally, depending on the lattice structure, different polytypes exhibit different stacking sequences. Thus, the cations or anions sublattice can be further categorized into different sublattices. When impurities occupy the lattice substitutionally, if both donors and acceptors substitute the cations or anion

sublattices, the type I donor-acceptor pairs are formed. Oppositely, the type II donor-acceptor pair formed when donors and acceptors substituted different ion sublattices separately[35, 36].
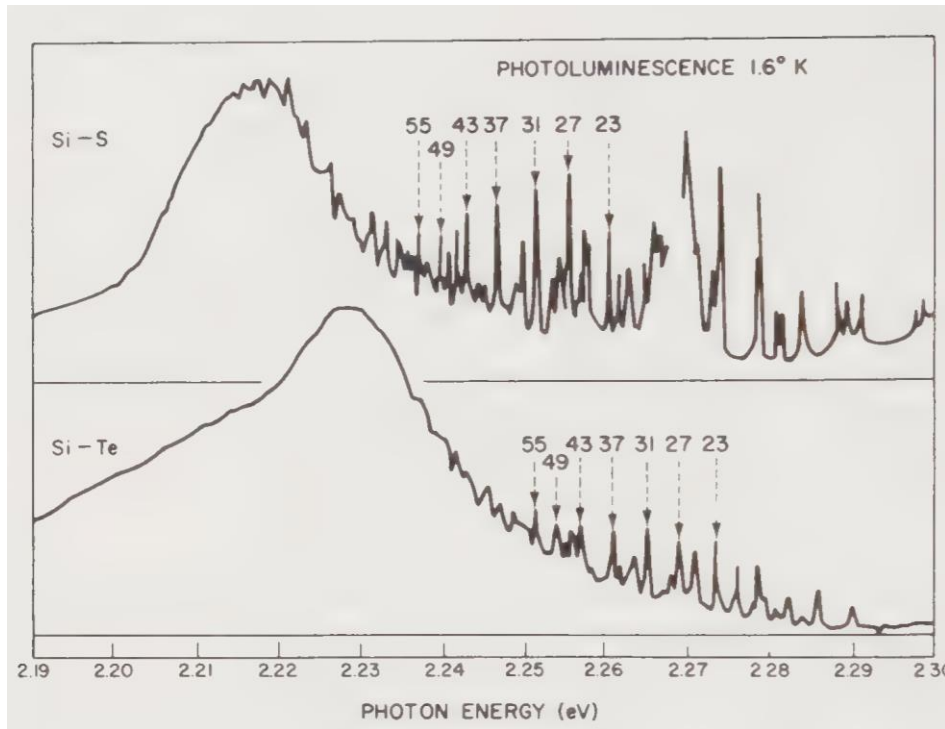
Figure 2.5 Photoluminescence spectra of Si-doped and Te-doped GaP at low temperature, showing isolated DAP pair peak respective to the separated distance[35].

The electron transitions among the impurities, which are separated by a distance larger than the effective Bohr radius, are achieved via tunneling. The probability of the transition decreases as the separation of impurities increases; thereby, the donor-acceptor recombination intensity follows a similar rule, and the intensity decreases as the separation increases. The example of GaP shown in Figure 2.5, a broad and the most intensive peak,

represents the recombination between DAP with a large separation. Also, several closely distributed pair emission lines can be found due to their specific spectral peaks. It is worth noting that each specific peak represents a shell with a set of possible sites for impurities. On the shell, the impurities share the same separation as the impurity located at the center.

2.5   Doping engineering

Doping is a common technique in the semiconductor industry to tune the electrical properties of materials. The dopant atom can either substitute sublattices in the host material or occupy interstitial sites. As shown in Figure 2.6, the donor and acceptor impurities form sub-energy levels within the bandgap of the host material. The recombination process between two dopant energy levels is referred to as donor-acceptor pair recombination(DAP). As an IV-IV compound semiconductor, SiC has multiple available options for dopants; the common p-type dopants include Boron (B), Aluminum (Al), and Gallium (Ga), then n-type dopants Nitrogen (N) and Phosphorus (P).

Dopants in 4H SiC	B	Al	Ga	N	P	V
Conductivity type	p	p	p	n	n	Semi-insulated
Ionization energy (meV)	580 for Si 300 for C	230	350	60 for hexagonal 120 for cubic	45(Hex) 80(Cub)	970 $\epsilon(0/1+)$ 1.97 $\epsilon(0/1-)$
Solubility (cm^{-3})	5×10^{19}	1.1×10^{21}	1.2×10^{19}	1×10^{20}	3×10^{20}	$3 - 4 \times 10^{17}$
Doping mechanism	Sub	Sub	Sub	Sub	Sub	Sub
Incorporated lattice site	Si or C	Si	Si	C	Si	

Table 2.1. Common dopants in 4H SiC and its fundamental properties [37-42].

In 4H-SiC, most common dopants fit into the host material crystal lattice substitutionally. Referring to Table 2.1, among the number of combinations of DAPs, recombination between Al-N and Al-P pairs produces emission wavelengths in the UV range. As for B-N and B-P pairs, the emission peaks are located in the range of green or yellow light. Here in this project, in order to obtain blue light emission via DAP recombination, the Ga-N DAP was selected due to its suitable energy differences for blue light phosphor application. Additionally, the phosphorus energy level in 4H-SiC is slightly shallower compared to the nitrogen level. In addition, phosphorus atoms have lower ionization difficulties than nitrogen atoms, which is undesirable for DAP recombination luminescence purposes.

The emission intensity of the DAP recombination strongly depends on the concentration of the DAPs. The ionization energies of Ga and N in 4H SiC are 0.35 eV and 0.09 eV,

respectively. Given that the ratio of cubic sites and hexagonal sites in 4H SiC is 1:1, therefore an approximation was made that assumes nitrogen atoms substitute cubic and hexagonal site carbon atoms uniformly, and the ionization energy of N is the average of two separate site levels[36].

As mentioned in the previous chapter, 2.4, the maximum emission peak of DAP exists between very distant pairs, where the coulomb interaction can be neglected. As a result, the most intensive emission peak energy of Ga-N DAP is given by:

$$E_{emission} = E_g - E_A - E_D = 3.26 - 0.35 - 0.09 = 2.82 eV.$$

The corresponding emission wavelength can be calculated using the following equation:

$$E = \frac{hc}{\lambda} \rightarrow \lambda = \frac{hc}{E} = \frac{6.626 * 10^{-34} J * s * 2.998 * 10^8 m/s}{2.82 * 1.61 * 10^{-16} J} \approx 435 nm$$

The emission wavelength is approximately equal to 435nm. The optimal dopant concentration for maximum recombination emission intensity is generally in the range of $10^{19} cm^{-3}$[16]. The concentration of donors needs to be slightly higher than the acceptor concentration since donors in 4H-SiC have relatively smaller ionization energy. At room temperature, donors can be easily ionized, which reduces the recombination intensity. By increasing the donor concentration, the Fermi level is raised into the conduction band, ensuring that donor states remain occupied by electrons. Thereby enhancing the recombination intensity.

Since a band-to-band transition in the indirect bandgap material must conserve both energy and momentum, the phonon provides the required momentum for electron-hole pairs (EHP) to complete the transition process. However, the phonons in the crystal can carry a broad range of momentum, which limits the transition rate of external excited EHPs. DAP recombination can be the solution to bypass the inefficient band-to-band transition based on the uncertainty principle:

$$\Delta x \Delta p \geq \frac{\hbar}{2}$$

Where x is the position and p is the momentum. Since the position of the impurity in the crystal lattice is certain, the momentum required for the transition will have a relatively larger range, which makes assistance from phonon for the recombination process no longer mandatory. Therefore, the EHPs have a larger probability of making radiative transitions.

Conduction band
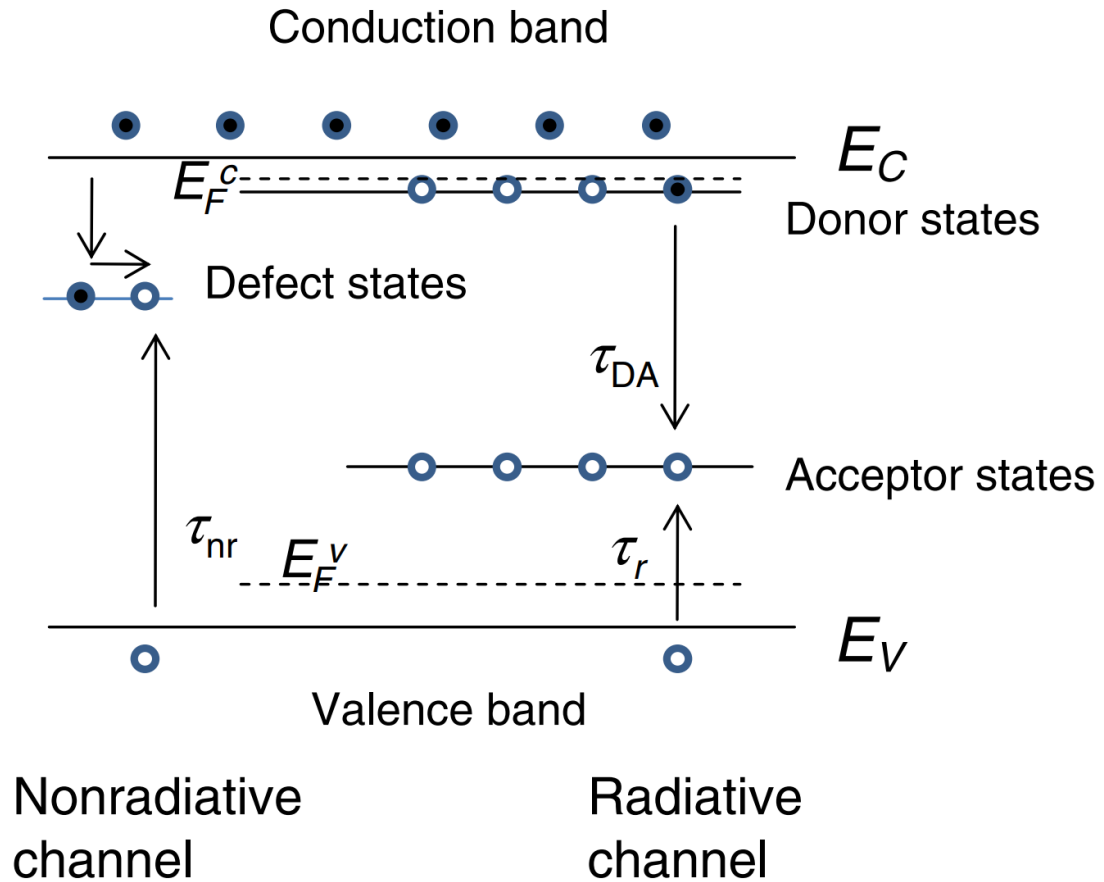
Figure 2.6. Schematic diagram of donor-acceptor pair energy level in the bandgap[36].

There are three viable methods to dope SiC: i) doping during crystal growth, ii) diffusion, and iii) ion implantation. In the crystal growth method, the dopants can be loaded into a crucible along with SiC powder, resulting in uniform doping throughout the crystal. However, to achieve maximum emission, a very high level of impurity concentration is required. At such high impurity concentrations, the conductivity of the crystal is too high to be used for a p-n junction application, which also deviates from the original goal of pixel-level luminescence control. Furthermore, doping SiC with high concentrations is relatively difficult, which requires very high temperature (generally> 2000K)[39]. Since

the Si-C bond in the SiC has one of the highest bond energy (4.6eV)[15], diffusion doping also requires a very high temperature to overcome the energy barrier. Especially for the p-type impurity, the diffusion temperature needs to in excess of $2000°C$. Lastly, the ion implantation is the most suitable technique for this project due to its precise spatial resolution, controllable projection depth, adjustable doping concentration and only requires a relatively lower activation annealing temperature[43]. When the ion are implanted into a crystal, the kinetic energy of ions are lost in form of elastic collision and electron excitation, inevitably generating Frenkel defects, As the defect density increases, the crystal can become amorphous[43].

2.6   Encapsulation & Passivation layer

Nitride-based materials such as AlN and SiN_4 have been widely used as passivation layers for various devices. The surface dangling bands are inevitable, which form by breaking the valence bond leaving unbonded electrons at the surface. The dangling bond wavefunctions can extend from the surface and create a surface state within the bandgap[31]. These dangling bonds can act as carrier traps and promote surface recombination. Surface defects generally have relatively large ionization energy, which competes with the DAP recombination. The most common method to passivate these dangling bonds is to form new bonds, which can be achieved by depositing an encapsulation layer or by annealing the sample in a hydrogen environment to form a hydrogen termination or immersing the sample into an acid solution. The key goal of the method is to tie up the dangling bond with extra electrons[11, 44].

In this project, surface passivation is crucial for two reasons. Firstly, the ion-implanted volume lies close to the surface (20nm depth). Based on the minority carrier diffusion length, the implanted volume lies within one diffusion length, which means surface recombination can be significant. Furthermore, post-implantation annealing is a critical step to recover the implantation damage and activate the impurities. Most p-type impurities in SiC require a minimum activation temperature of around 1600℃. However, once the temperature exceeds 1400℃, the silicon in SiC starts to evaporate, which results in surface roughening and leaves dangling bonds at the surface. The erosion can also damage the implanted region. Thereby, the encapsulation layer must provide surface passivation and thermal stability at high temperatures.

$$L = \sqrt{Dt} = \sqrt{4.2cm^2/s * 2.1us} = 29um \ [45, 46]$$

AlN, graphite, and BN are the three available candidate materials for the encapsulation layer. AlN is more commonly used compared to graphite and BN because of the relatively lower deposition difficulty. Although BN exhibits better thermal stability at higher temperatures (>1700℃), the abnormal diffusion coefficient of boron creates an unwanted boron-doped region. Due to the larger binding energy, the boron energy level can hamper the recombination process of the Ga-N pair. On the other hand, Al in-diffusion does not result in a significant impact on the recombination because of the lower binding energy among the three common p-type impurities[37].

Additionally, AlN passivates the surface by forming charges at the interface. As a well-known piezoelectric material, AlN can generate a directional electric field at the interface.

Depending on the crystal orientation, the electric field typically points from the N-face toward the Al-face along the c-axis. The deposition process starts with silicon atoms that bond with nitrogen atoms, followed by sequential stacking. The spontaneous electric field at the interface repels the electrons, thus suppressing surface recombination. Therefore, in this project, the Si-face of the SiC substrate was selected for Ga doping. Part of the passivation effect is attributed to the charged defects generated during the deposition process near the AlN/SiC interface. The charge accumulation starts at the first 4nm of the AlN layer deposition, and then the effect of the charges is reinforced by the presence of a thin oxidation layer and the subsequent annealing process[11]. The enhancement likely arises from Al diffusion at high temperatures, creating Al vacancies and Al oxides that contribute to the electric field at the interface.
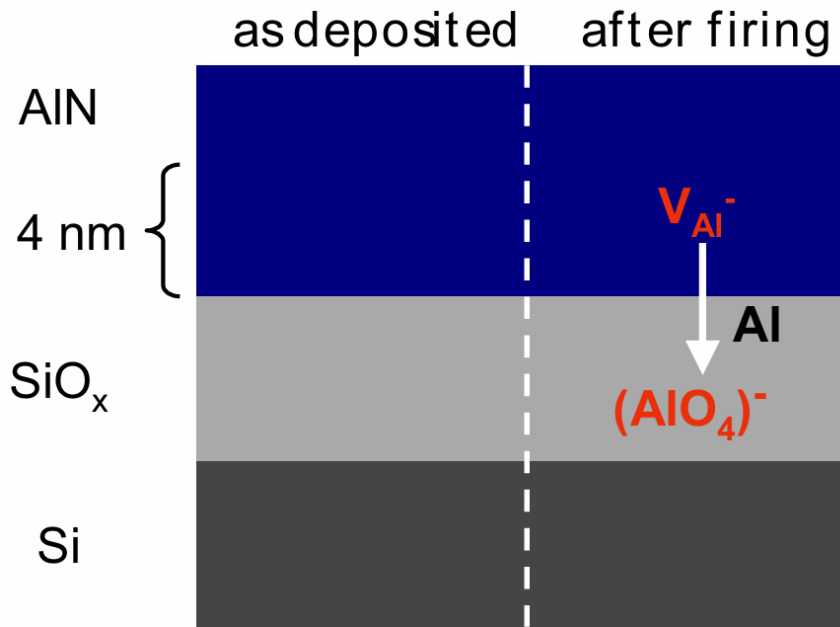
Figure 2.7. Schematic diagram of AlN defects induced charges, interaction takes place between AlN and oxide layer, aluminum vacancies form by aluminum redistribution during the annealing enhance the electric field intensity[11].

2.7 Carbon defects in SiC

The surface defect originating from the surface roughness in the SiC can result in a high surface recombination rate and hamper the carrier recombination in the DAP pair. The carbon-related defects at interfaces are particularly pronounced types among the surface defects in SiC[47]. The carbon-related defects include carbon vacancies and carbon interstitials, where the carbon vacancies are primarily responsible for the carrier lifetime reduction[48]. The carbon vacancy can introduce an energy level of 0.9eV above the valence band. The vacancy density can be reduced by using carbon ion implantation and rapid thermal oxidation methods. The major defect energy level can be eliminated via a

carbon self-ion implantation mechanism by thermally oxidizing at $1150 - 1300°C$ and ly annealing in an Ar environment at $1550°C$ sequentially[49]. The ion implantation into SiC can also generate silicon vacancies, which result in suspended bonds on the neighboring carbon atoms. The silicon vacancies form a promising prospect in the field of quantum computing due to their half-integer spin, photostability, and long spin time at room temperature[50]. Lastly, carbon interstitials can significantly influence doping diffusion during the ion implantation and annealing processes[50].
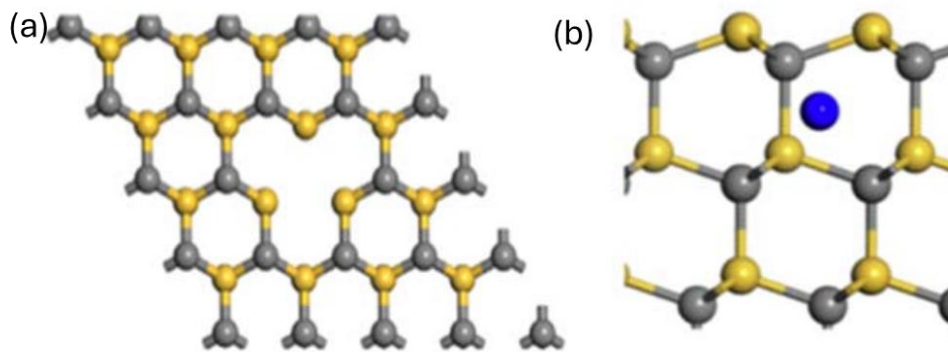
Figure 2.8. Carbon-related defect in SiC (a)carbon vacancy (b)carbon interstitial, grey-C atom, yellow-Si atom[50].

3 Chapter 3: Materials & Methods & Characterization

3.1 Samples preparation methods

The project begins with a substrate, which is a single crystal 4-inch n-type 4H-SiC wafer with a thickness of 350μm, purchased from MSE Supplies. The wafer was diced into smaller pieces with a dimension of 1×1cm. The substrate is nitrogen-doped with a concentration $10^{18}cm^{-3}$. The wafer underwent chemical mechanical polishing on both Si-face [0001] and C-face [000-1] with the specified roughness of Ra 0.5nm. The wafer was cut with 4-degree misorientation toward [11-20] by the manufacturer.

At the beginning of the experiment, all the substrates were carefully cleaned with RCA cleaning process as follows (refer to Figure 3.1): (1) ultrasonication sequentially in acetone, methanol, and isopropanol for 5 min each. (2) 15 mins in $H_2SO_4: H_2O_2 = 1:1$. (3) 15 min in 70℃ $NH_4OH: H_2O_2: de-ionized\ water(DIW) = 1:1:3.3$. (4) 15 min in 70℃ $HCl: H_2O_2: DIW = 1:1:3.3$. And rinsing the sample with DIW and drying it with N_2 gas after each step. After each of steps 2, 3, and 4, samples were cleaned in 10% HF for 5 min, then rinsed and dried with nitrogen gas[51, 52].
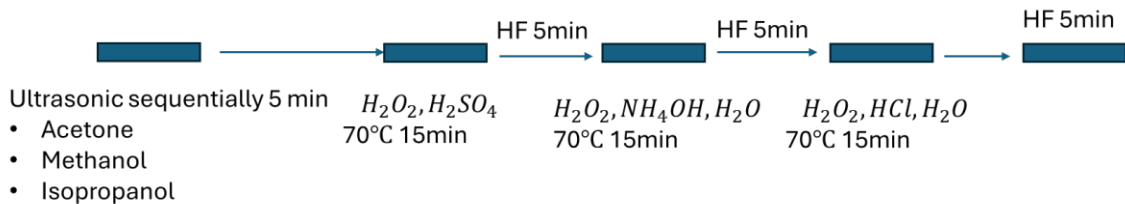
Figure 3.1. Wafer cleaning procedures

Ultra shallow ~20nm   [002] AlN Thin Film~400nm   Flip and cover for annealing at 1600°C In CLAM furnaces

Ion Implantation—FIB   Reactive Sputtering 2 inch Al Target   SiC Wafer

Figure 3.2. Schematic diagram of Ga implantation and activation process

As depicted in Figure 3.2, after the cleaning, the ion implantation process was completed with the assistance of a Thermo Fisher Helios 5 UC ion milling machine at room temperature. The acceleration voltage applied to the gallium ion was 30kV. The implanted areas have square geometry with a size of 100×100um or 200×200um, the implantation dosage is $67.78 pC/um^2$, Ga concentration was approximately equal to $10^{22} cm^3$ by calculating the implantation depth.

After the ion implantation step, the samples were immersed in a 5% HF solution to remove the oxidation layer, contamination, and particles unintentionally sputtered during the implantation process. After the HF cleaning, the surface dangling bonds were exposed, which provides better adhesion for the following deposition process. Immediately after cleaning, the samples were loaded into a sputtering chamber, and a 400nm AlN encapsulation layer was deposited upon the Si-face using the reactive magnetron sputtering method with the assistance of an Angstrom Science ONYX-02IC Standard Magnetron sputtering gun fitted with a 2-inch aluminum target. The base pressure in the chamber was pumped to $5 \times 10^{-6} Torr$ to minimize oxygen, moisture, and hydrocarbon contamination. The deposition was completed at 175W sputtering power with a 5 mTorr sputtering

pressure at room temperature. During the deposition, the substrate temperature rose due to the plasma heating at very close proximity (3cm, from target to substrate). The sputtering gas had the composition of $Argon : Nitrogen = 1 : 3$, with a total gas flow rate of 52 sccm.

After the deposition, the samples were loaded into a Coded light-sheet array microscopy (CLAM) confocal microscope furnace in an alumina crucible. The samples were flipped and placed on a fresh SiC wafer to mitigate the decomposition of AlN by increasing the partial pressure between the two wafers. As shown in Figure 3.2, the implanted region and AlN encapsulation layer were sandwiched between two SiC wafers. Prior to the annealing, the furnace chamber was pumped down and then backfilled with Ar gas for three cycles. Then, the samples were annealed for 15min at 1600℃ in an Ar environment.

Figure 3.3. UV Photoluminescence and UV-visible photodetector spectroscopy system.

3.2   Characterization methods

3.2.1. Photoluminescence

The photoluminescence (PL) technique was used to probe optical properties and emission peaks corresponding to the defect states in the material. In this project, samples were excited with a Coherent OBIS 375 nm He-Ne laser. During the testing, abundant electron and hole pairs form in the material, and then the photogenerated carriers migrate towards the sub-energy level, such as donor, acceptor, and defect energy. Afterward, the radiatively recombined carriers emit photons, which were detected by an Ocean Optics UV-to-VIS spectrometer. Since the excitation source has a wavelength of 375nm, a light filter was deployed to filter out the incident light blocks wavelengths shorter than 400nm.

3.2.2. Cathodoluminescence

The Cathodoluminescence (CL) spectrum was carried out by using a Thermoscientific Quattro environmental scanning electron microscope (ESEM) system equipped with an Odemis CL detector from Delmic. Similar to the PL spectrum, the CL spectrum was used to characterize the energy level and optical properties of the samples. Instead of a laser, CL uses an electron beam as the excitation source. The electron beam is generally more energetic than a light beam. Unlike PL increasing carrier concentration by generating EHP, the electrons can be injected into the conduction band of the material. Therefore, CL has the potential to excite and observe the energy levels that cannot be easily excited by PL.

3.2.3. Transmission Electron Microscopy (HRTEM)

The material composition, depth profile of the implanted region, high-resolution morphology, and crystal structure were obtained by applying a TFS Spectra Ultra TEM system. The composition and structural information were collected with the help of Energy Dispersive X-Ray Analysis (EDX) and electron diffraction techniques respectively. The cross-section area was selected since ions were implanted perpendicularly into the substrate. The high-quality TEM samples were prepared with the assistance of a Helios 5 plasma-focused ion beam (PFIB) system with an Xe source, which avoids unintended Ga contamination during the sample lift-up and thinning process.

3.2.4. X-ray diffraction

The AlN thin film crystal orientation and texture were probed with the assistance of X-ray diffraction to determine the optimal sputtering parameters by analyzing the crystal orientation. The incident X-ray has the wavelength 1.5405Å, which is generated with a Cu target. All AlN samples were deposited on the Si-face 4H-SiC with various sputtering parameters and the same sputtering time.

3.2.5. Raman Microscopy

InVia Micro-Raman Microscopy manufactured by Renishaw was used to characterize the damage induced by implantation evolution with different activating annealing conditions. The impurity distribution in heavily doped SiC is often inhomogeneous, which can lead to changes in the local electric properties. As a well-known non-invasive surface

characterizing method, Raman spectroscopy has been widely used for analyzing polar semiconductor material properties[53]. The longitudinal optical phonon plasmon coupled (LOPC) modes in SiC can be used as an indicator to estimate the free electron concentration and net donor concentration $(N_d - N_a)$ on the surface [53]. As the free carrier concentration increases, the LO mode becomes broader and shifts in frequency. These changes are attributed to the phonon-plasmon coupling via an electric field. There are two LOPC branches, which are L- and L+. As the free carrier concentration increases, the L-branch frequency shifts from 0 to Transverse optical phonon frequency. For the L+ branch, which is usually used for carrier concentration calculation, the frequency shifts from the LO mode frequency to the plasma frequency. However, the low mobility and large effective masses of plasmons in SiC cause the two branches of LOPC to become mixed together due to the overdamping[53, 54]. Therefore, the estimation of free carrier concentration has to be calibrated mathematically.

Figure 3.4 shown the empirically estimated relationship between LO position and doping concentration. Therefore, the Raman results collected from the samples can be compared with the empirically obtained values to estimate the net carrier concentration and Ga activation ratio. In this project, the 532nm laser with 50% power was selected as the source for Raman spectroscopy. The alignment was completed with the assistance of built-in optical microscopy.
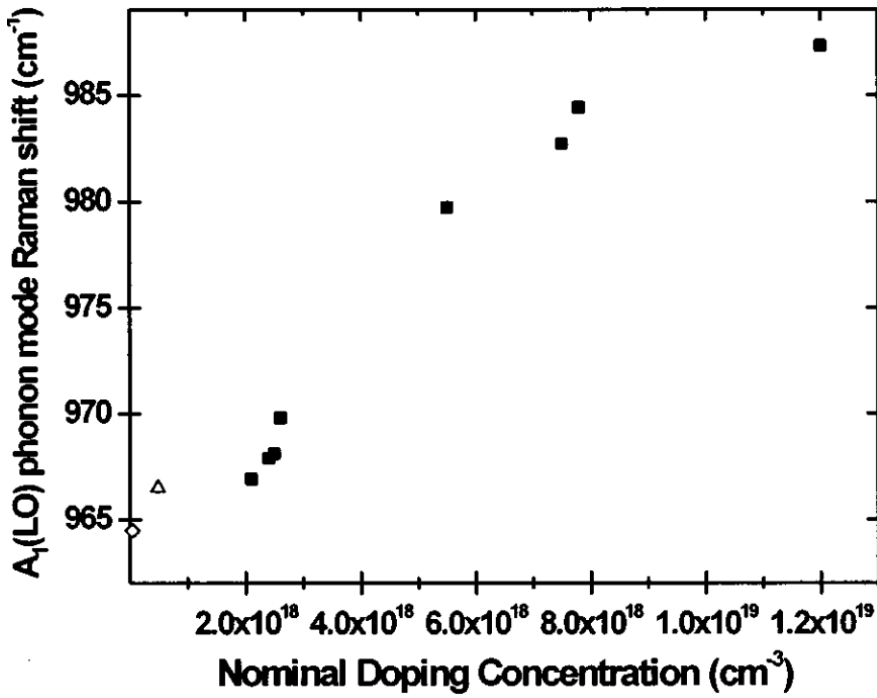
Figure 3.4. Average LO mode position vs. Nominal nitrogen doping concentration in 4H-SiC[54].

3.2.6. Scanning electron microscopy

Scanning electron microscopy (SEM) and SEM Energy Dispersive X-ray analysis (EDX) were performed using an FEI Magellan 400 system. The morphology and preliminary composition information were collected using this SEM system.

4 Chapter 4: Results and Discussion

4.1 Transport of Ions in Matter (TRIM) Simulation
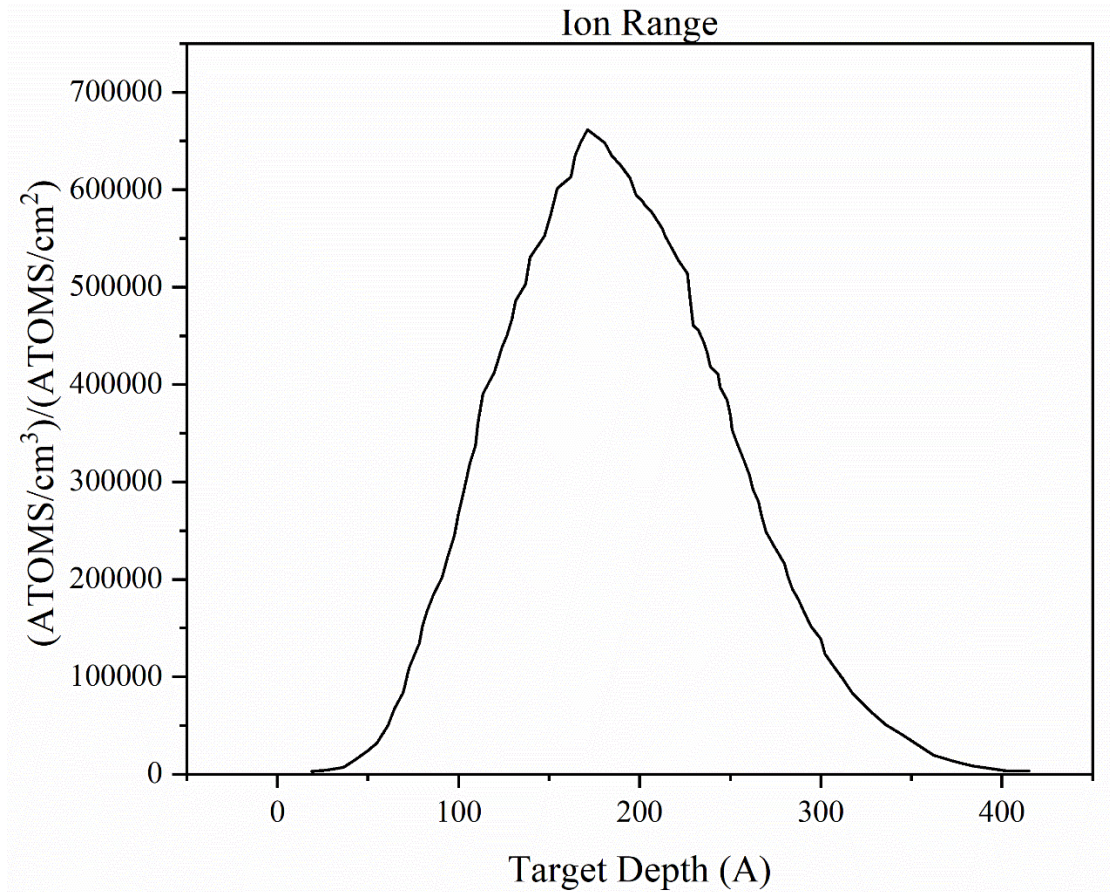
Figure 4.1. Simulation results of Ion distribution vs. Depth for Ga-implanted 4H-SiC at 30kV acceleration voltage.

The ion distribution and depth profile of Ga ion implantation were simulated by using TRIM (Transport of Ions in Matter) and SRIM (Stopping and Range of Ions in Matter) software. The simulation result is depicted in Figure 4.1. A simple assumption was made for the simulation: the substrates have a density of $3.21 g/cm^3$, and threshold displacement energies for Si and C sublattice are 35eV and 20eV respectively[55]. Referring to the

diagram, the ion projection range of gallium atoms in 4H-SiC with a 30kV acceleration voltage is approximately 20nm, with the tail of the projection extending to 40nm below the substrate surface.

4.2   SIMS result
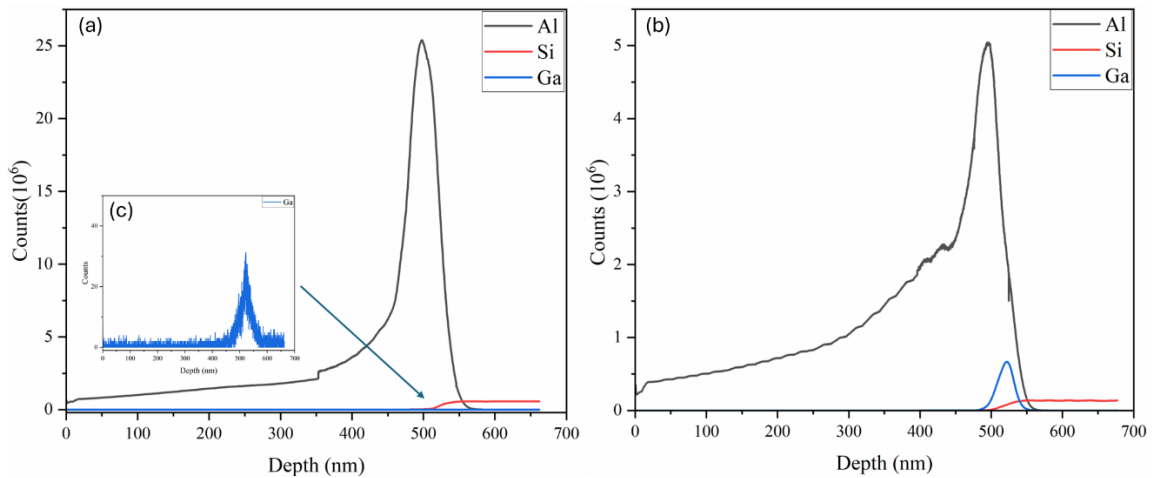
Figure 4.2. SIMS results for Sample annealed at 1600℃ 15mins. (a) Undoped region (b) implanted region (c) Undoped region Zoom-in.

The secondary ion mass spectrometer (SIMS) was used to determine the concentration of the major elements. Cesium ions were selected as the source for measurements. During the testing, the surface of the sample was bombarded with cesium ions, and the atoms from the sample were sputtered from the surface and detected by a mass analyzer. Hence, the elements' concentrations were calculated based on the atomic weight.

The SIMS results are depicted in Figure 4.2(a) and (c). In the result from the undoped region, a trace amount of Ga can be detected at the SiC/AlN interface, indicating that the Ga atoms have a higher diffusion coefficient at the interface. The Al in-diffusion can be

observed on both regions within a range of tens of nanometers. Similarly, as shown in Figure 4.2 (b), the diffusion length of Ga is in a range of 50nm below the SiC surface after the annealing process. An abundant amount of Ga is accumulated at the SiC/ AlN interface, suggesting that the AlN capping layer successfully slows down the Ga out diffusion tendency and increases the Ga concentration gradient at the interface, thereby promoting Ga in-diffusion into the SiC substrate.

4.3 AlN deposition

After the ion implantation, the optimal activation annealing temperature for 4H-SiC is around 1600℃-1700℃ to allow Ga to fit into the lattice substitutionally and repair the crystal lattice damages induced during the implantation. As mentioned in the previous chapter 2.6, the implanted region can suffer from the erosion of Si evaporation and Ga out-diffusion.

In order to obtain the optimal protection for the implantation region, AlN with [0002] crystal orientation is desired. Along the [0002] crystal orientation, wurtzite structured AlN is densely packed. Thereby, the interlayer diffusion of gallium can be minimized.

Table 4.1 summarizes the samples with various sputtering conditions. Based on the SEM result shown in Figure 4.3 and Figure 4.4, as deposition temperature increases, the grainy morphology transfers into a flat surface with many pits, which may indicate inadequate adhesion between the substrate and the deposit. The SEM-EDS results partially reveal the underlying transformation. The oxygen content increases from 35 at% to 42 at% as the temperature rises from 300℃ to 350℃, and the worm-like morphology suggests that the

41

film may consist of alumina. Although the Al-N reaction rate increases with temperature, the rising temperature may also intensify the reaction between Al and O, as Al atoms are highly sensitive to oxygen. Additionally, the substrate may oxidize during the substrate pre-heating procedure, and resulting silicon oxidation deteriorates the surface condition, ultimately causing an adhesion issue.

Sample #	Power (W)	Pressure (mTorr)	Targets	Substrate Heating (℃)	Gas Composition $N_2 : Ar$
S11	65	15	AlN	300	100:0
S13	65	20	AlN	350	100:0
S17	100	20	Al	RT	65:35
S20	100	5	Al	RT	65:35
S23	100	10	Al	RT	65:35
S28	200	10	Al	RT	65:35
S33	150	20	Al	RT	65:35
S36	175	5	Al	RT	75:25

Table 4.1. Summary of AlN samples with different sputtering parameters.
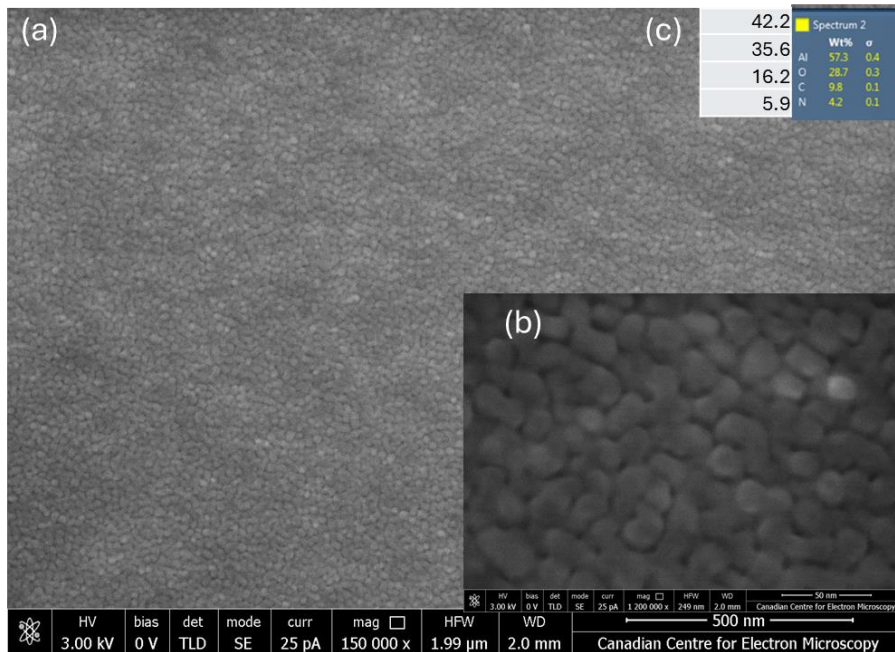
Figure 4.3 Sample 11(65W, 15mTorr, 300℃, pure N_2) (a) Overall surface morphology image (b) Zoom-in surface morphology (c) EDS result in at% and wt%.

By comparing the SEM image, samples prepared with an Al target exhibit a more uniform grain structure compared to the samples prepared with an AlN target. The oxygen contamination in the Al target-prepared samples is significantly lower than in the samples prepared by the AlN target. The high oxygen concentration is attributable to the lower deposition rate caused by RF sputtering and the use of an AlN target. In a typical RF sputtering voltage cycle, only half of the cycle contributes to the growth, and the lower thermal conductivity and expansion of the AlN target limit the maximum power that can be applied during the sputtering. The lower deposition rate causes the Al atoms to be more likely to interact with the oxygen in the chamber. There are several sputtering parameters

that significantly affect the deposition rate: substrate to target distance, power, sputtering pressure, flow rate, base pressure, and sputtering temperature.
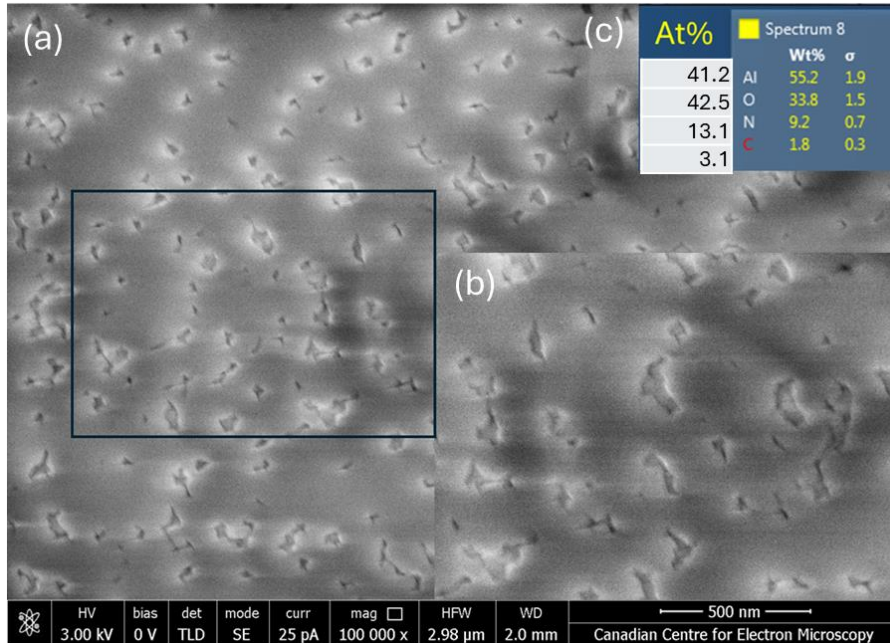
Figure 4.4. Sample 13 (65W, 20mTorr, 350°C, pure N_2) (a) Overall surface morphology image and pits (b) Zoom-in morphology in selected region (c) EDS result in at% and wt%.

The deposition rate is inversely proportional to the square of the distance, power decides the sputtering rate, and operating pressure influences the scattering distance of the atoms. Referring to the literature, samples prepared with a higher sputtering chamber gas flow rate tend to have lower oxygen contamination[56].

Referring to Figure 4.5 and Figure 4.6, the polycrystalline morphology and columnar structure at the cross-section indicate that the crystals are highly c-axis oriented. However, remarkable oxygen contamination can still be observed in the EDS results for Sample 17.

By decreasing the sputtering pressure in Sample 20, the oxygen concentration decreases dramatically, and the aluminum to nitrogen ratio is approaching 1, indicating the film is primarily composed of AlN. The morphology of Sample 20 changes from a grainy shape toward a spindle structure at the surface, which generally reflects that the crystals are primarily [101] oriented. The cross-section image presents a structure transformation from a columnar structure at the interface to a lamellar structure at the top. This transformation may be caused by the lattice mismatching. The AlN lattice structure may have the same structure as SiC at the initial stage and then gradually transition into a uniform structure due to the lattice relaxation. The substrate self-heating may also promote the transformation of crystal structure. The stress and mismatch may be intensified due to the thermal expansion.
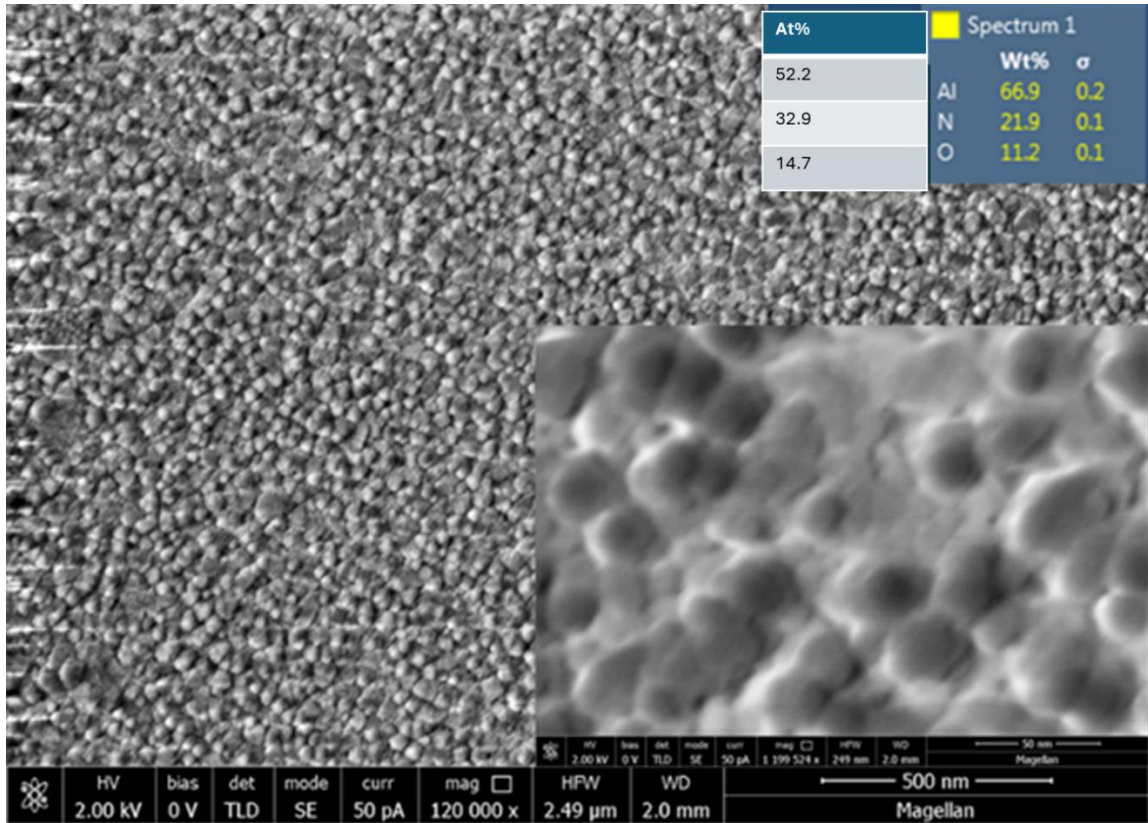
Figure 4.5.Sample 17(100W, 20mTorr, RT, Ar:N_2 =35:65) (a) Overall surface morphology image (b) Zoom-in morphology (c) EDS result in at% and wt%.
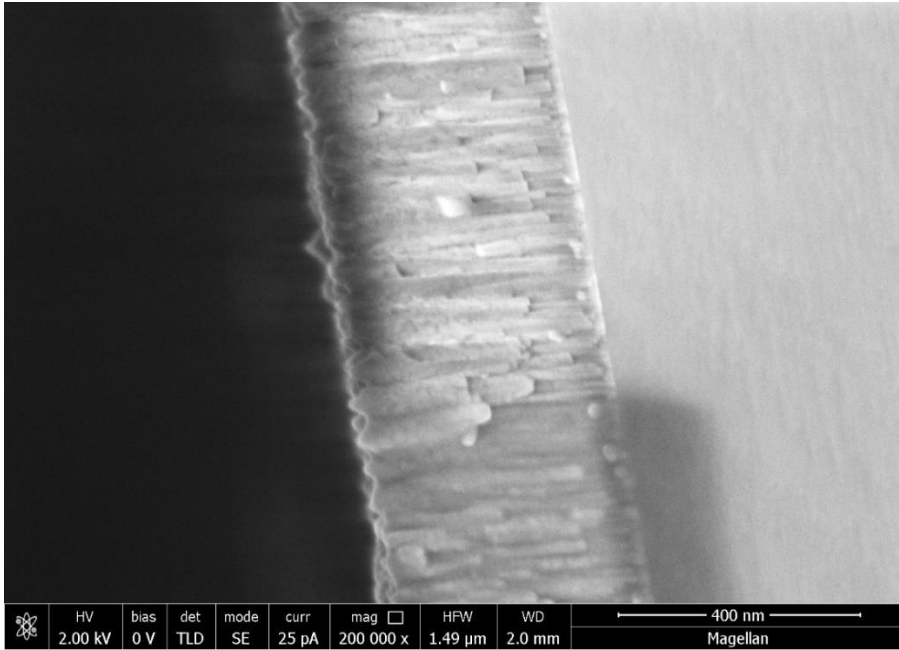
Figure 4.6. Sample 17 Cross-section, column grain structure along the c-axis.
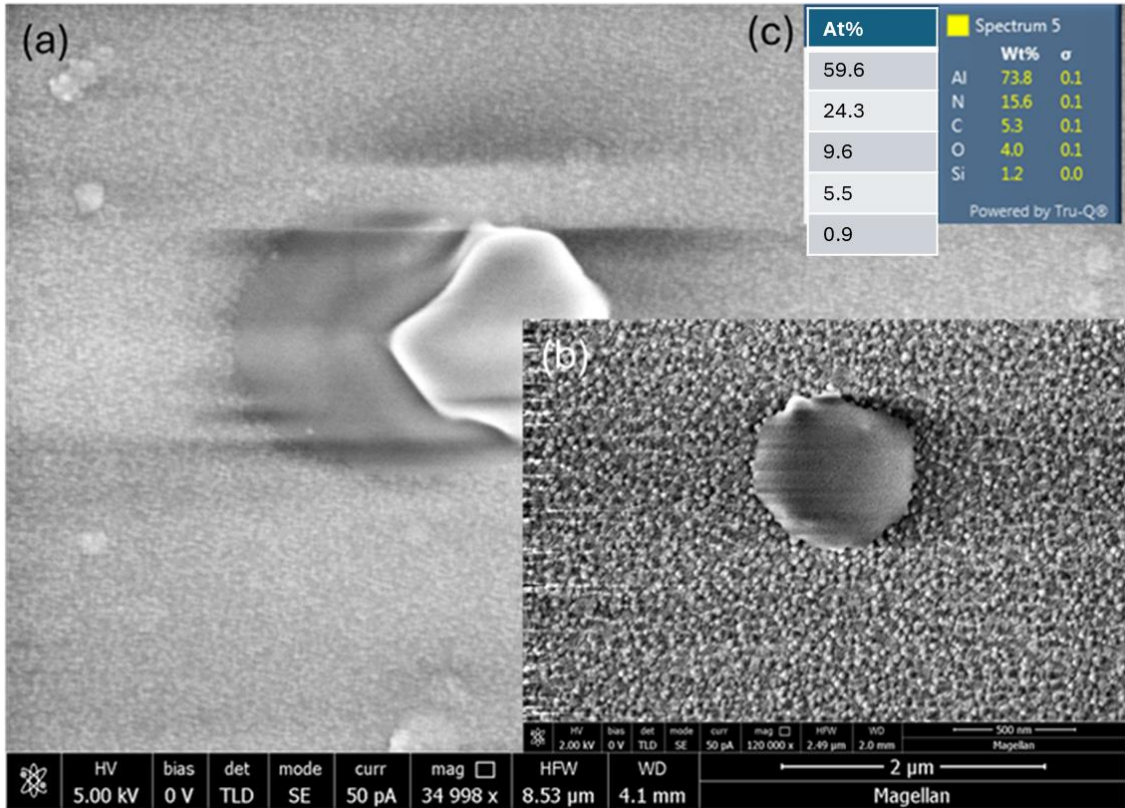
Figure 4.7. Sample 17, Al particles. (a) Overall image for Al particle at the surface (b) Zoom-in image for Al particle(c) EDS results in at% and wt%.
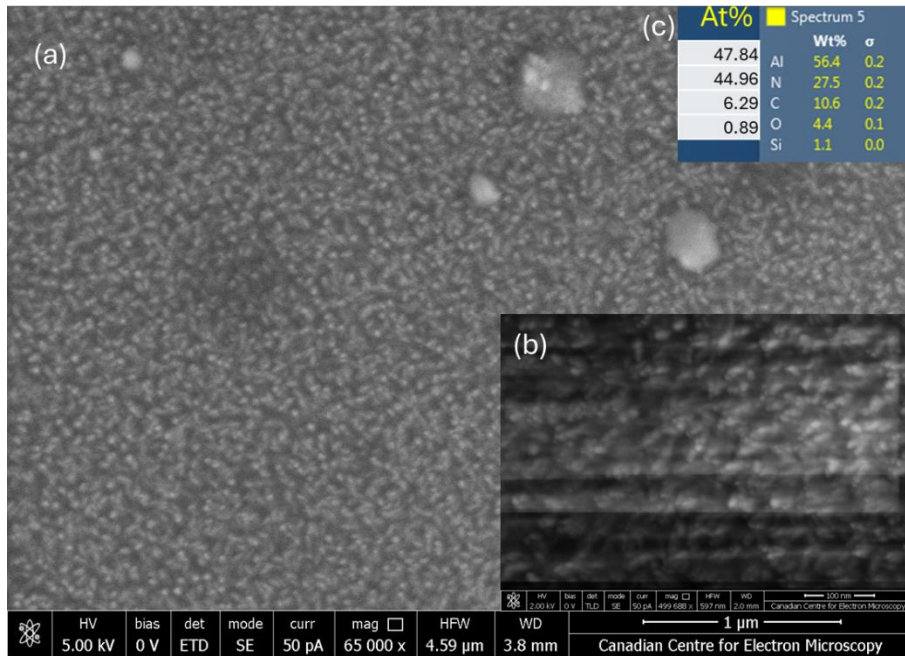
Figure 4.8. Sample 20(100W, 5mTorr, RT, Ar:N$_2$ =35:65) (a) Overall surface morphology (b) Zoom-in morphology of spindles shape grain structure (c) EDS result in at% and wt%.
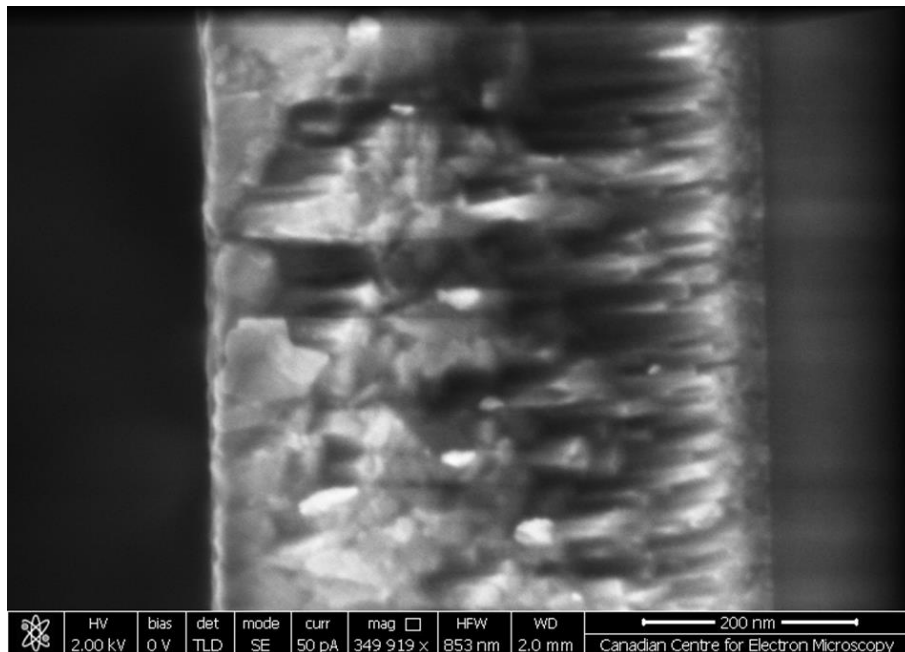
Figure 4.9. Sample 20 Cross-section, bottom column structure, non-uniform substrate independent structure.

Aluminum particles can be found on both Sample 17 and 20. These particles could potentially affect the quality of the AlN encapsulation layer and the subsequent annealing process. The deposition of particles is caused by arcing. Aluminum can interact with oxygen or nitrogen and form an insulating layer on the surface, which leads to the arcing effect. When the arcing effect takes place, the Al particles are ejected from the target and deposited onto the substrate. Adequate pre-sputtering cleaning can be the solution of arcing. The sputtering duration is another important factor that may cause arcing. As sputtering progresses, nitrogen may also form an AlN film on the target, leading to arcing. Based on the experimental observation, a single sputtering cycle should be controlled to within 20 minutes to obtain an optimal particle-free morphology.
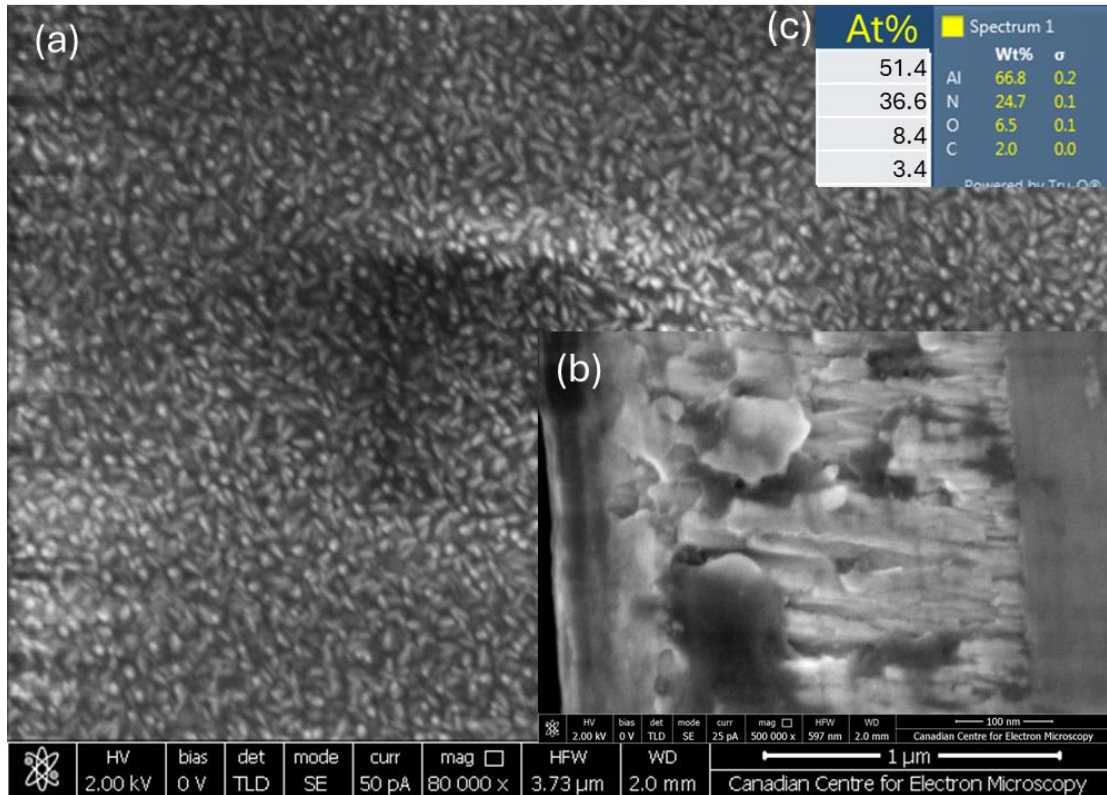
Figure 4.10. Sample 23 (100W, 10mTorr, RT, Ar:N$_2$ =35:65) (a) surface spindle morphology (b) cross-section, flake-like structure (c) EDS result in at% and wt%.

The samples prepared with intermediate pressure are presented in Figure 4.10 (a). The spindle structure at the surface of Sample 23 is less dense than in Sample 20, which agrees with the literature as follows: Highly c-axis oriented [0002] AlN requires lower reaction energy compared to [101] or [111] oriented AlN[57]. Therefore, the evolution of the sputtering parameters should aim to minimize sputtering energy to ensure c-axis oriented crystal. However, due to the capability of the sputtering chamber, the minimum base pressure that can be achieved is in a range of $10^{-6}Torr$. This is two orders of magnitude

higher than the typical base pressure of 10^{-8} Torr used in most nitride material deposition conditions[57, 58]. The higher base pressure results in increased oxygen contamination in the deposited film. A higher deposition rate can effectively reduce the reaction between aluminum and oxygen. Increasing the power, argon composition, and decreasing the pressure can effectively increase the deposition rate of AlN, but higher deposition rates deliver more energy to the substrate, which inevitably affects the crystal orientation. Therefore, it is important for this project to identify the optimal sputtering parameters that minimize oxygen contamination while maintaining as much [0002] oriented AlN crystal as possible.

Referred to the Figure 4.11, Figure 4.12 and Figure 4.13, the sputtering parameters used to prepare Sample 36 were selected for later experiments, as these samples have the lowest oxygen concentration and crystals are generally oriented in the [0002] direction.
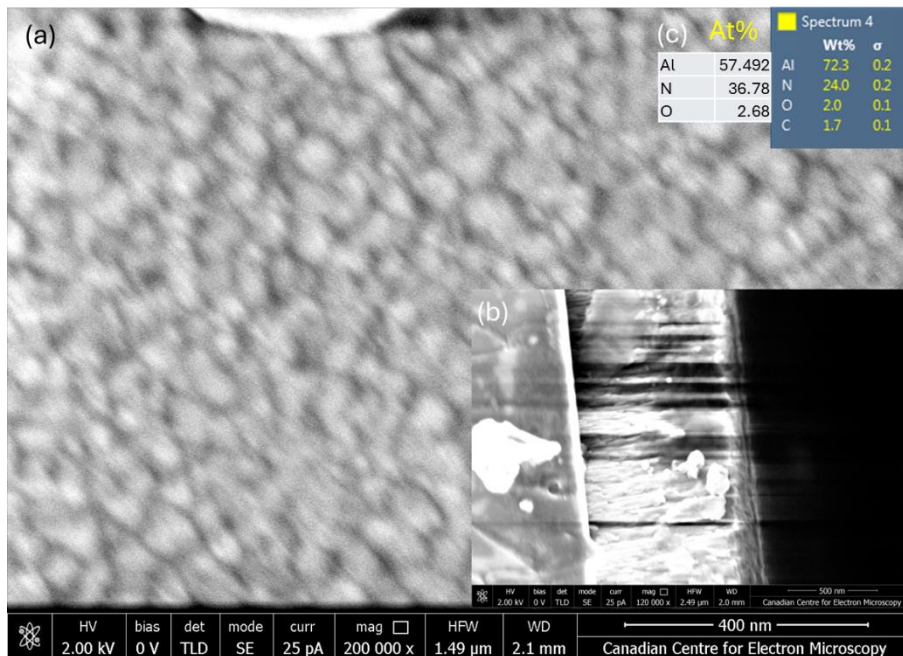
Figure 4.11. Sample 28(200W, 10mTorr, RT, Ar:N$_2$ =35:65) (a) Overall surface morphology (b) cross-section image (c) EDS result in at% and wt%.
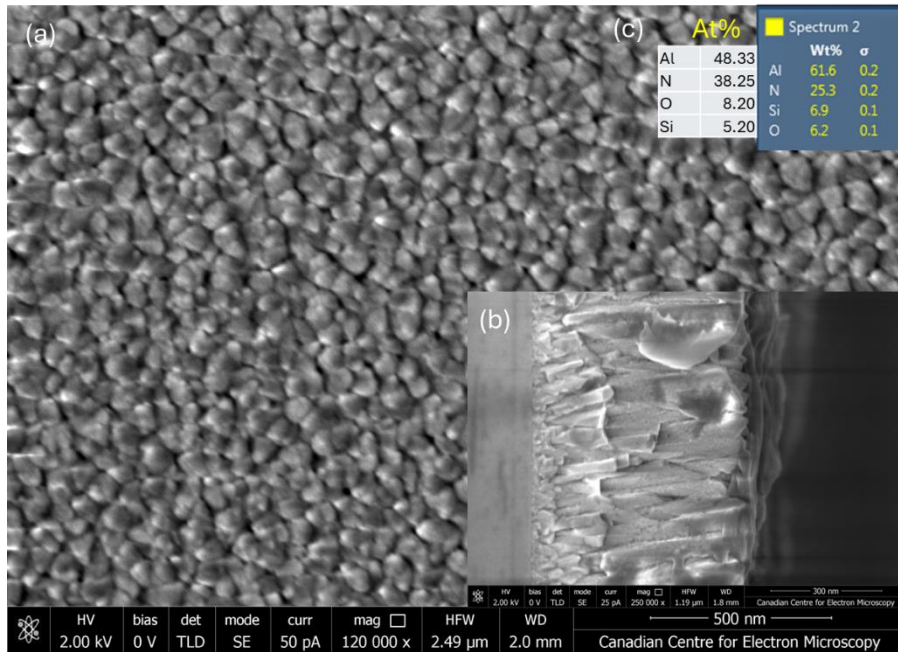
Figure 4.12. Sample 30 (150W, 20mTorr, RT, Ar:N$_2$ =35:65) (a) grainy surface morphology(b) cross-section, column structure at the bottom, flake-like structure on the top(c) EDS result in at% and wt%.
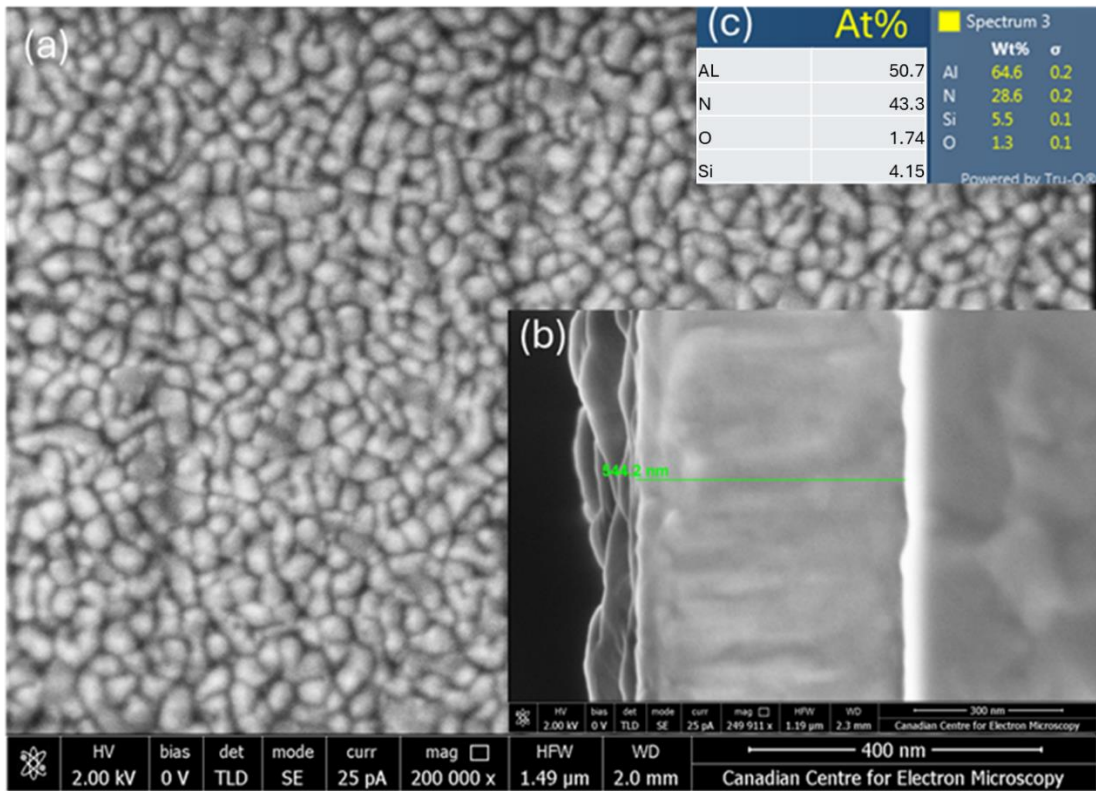
Figure 4.13. Sample 36(175W, 5mTorr, RT, Ar:N$_2$ =25:75) (a) Overall (b) Zoom-in (c) EDS result in at% and wt%.
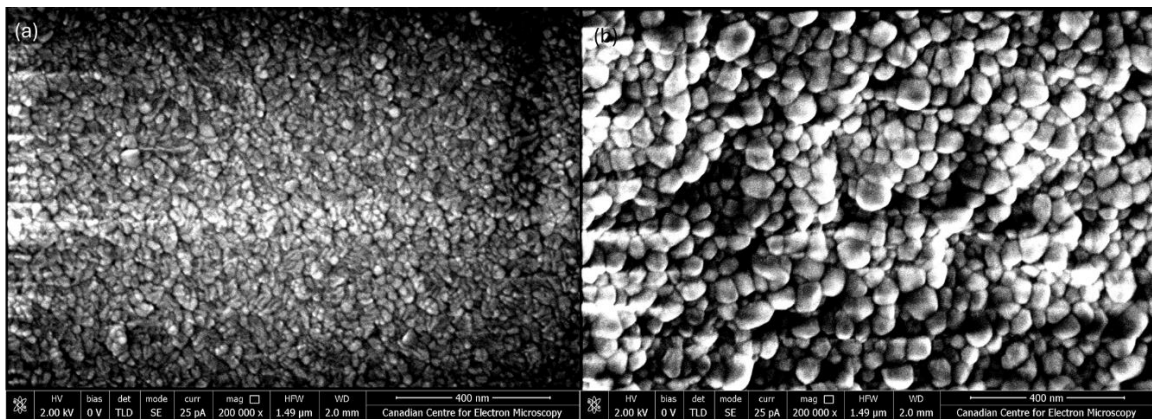
Figure 4.14. SEM morphology image of AlN layer (a) as-deposited (b) 15min annealing at 1600℃.

According to Figure 4.14, the AlN experienced intensive recrystallization during the annealing process. The crystal size on the annealed sample is much larger than that in the as-deposited sample.

4.4   EDS results as implanted
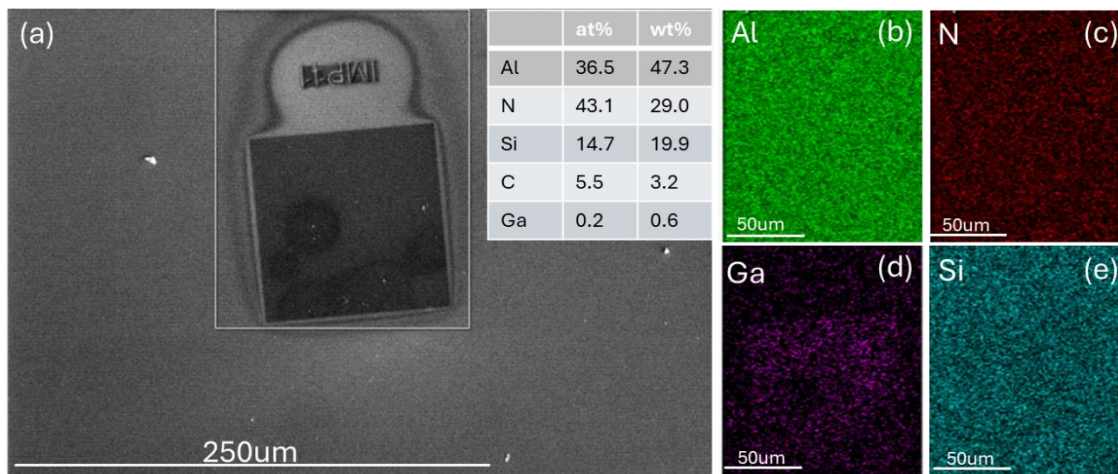
Figure 4.15. SEM-EDS mapping result for Ga-doped SiC region after 1600℃ annealing. (a) SEM image for mapping area. (b) Al. (c) N. (d) Ga. (e) Si.

The EDS results are depicted in Figure 4.15. The mapping results of the Ga implanted region were measured using SEM-EDS after a 1600℃ 15-minute activation annealing. The implanted region has a geometry of 100um*100um. After the annealing, the implanted region appears to have a darker contrast compared to the un-implanted region. The contrast difference may suggest a change in surface morphology or crystal damage induced by implantation. Part of the SiC was milled away during the implantation process due to the

sputtering effect. Referring to the figure, the distribution of Ga atoms roughly remained within the same square region as the implantation. Several darker regions can be observed within the square. These regions appear to have AlN layers that are either peeled off or cracked during the annealing process. The Ga signal is also absent from these darker regions in the EDS results, suggesting substantial Ga out-diffusion after annealing.

4.5   XRD results
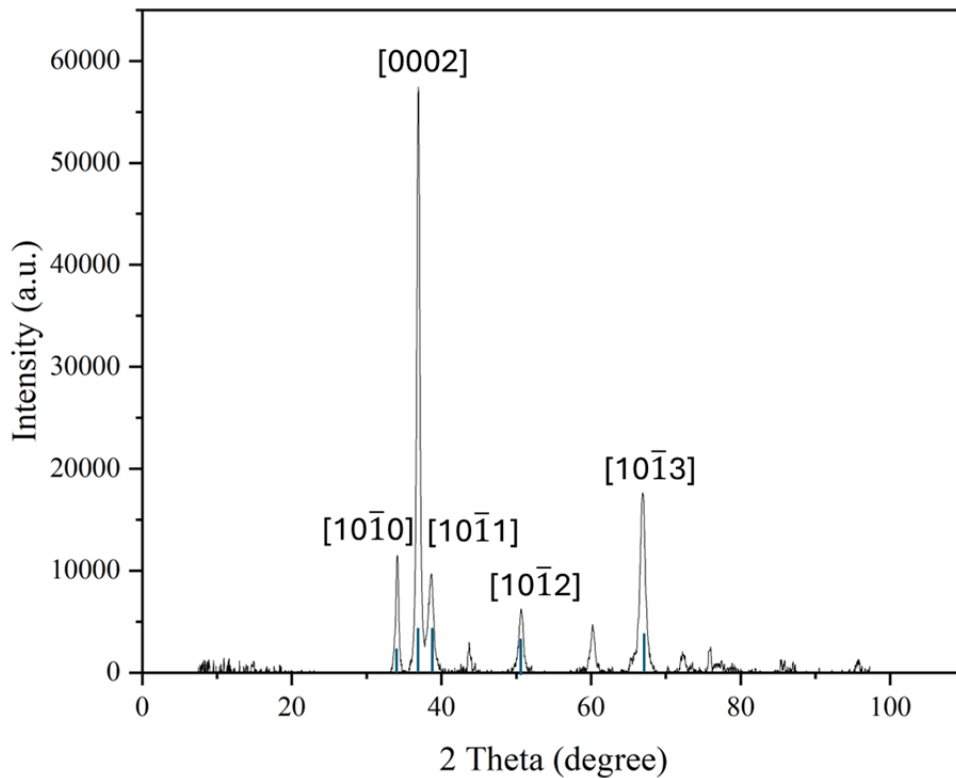
Figure 4.16. XRD results for as-deposit AlN film.

The signal from the [0002] orientation became more intense after annealing, which suggests that the [0002] orientation is more thermodynamically favorable at elevated temperatures. The polar figure in Figure 4.17 reveals that the crystal exhibits a certain

amount of tilt around its orientation. The points on the hemisphere represent the crystal orientations of the substrate, while the surrounding rings represent the crystal orientations of the AlN film. The multiple rings indicate a relatively large distribution of crystal tilting in the film.
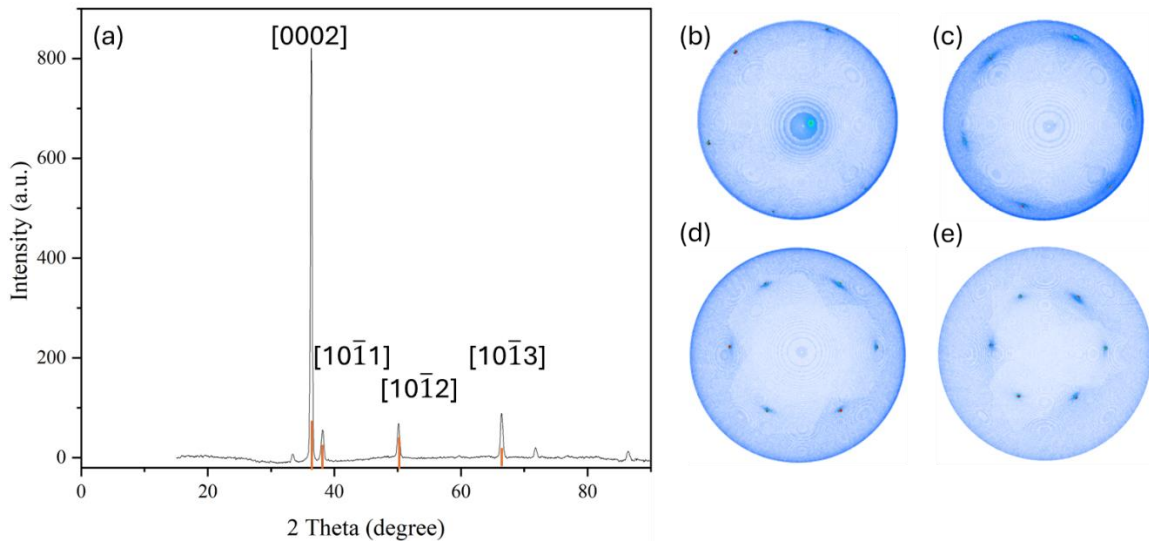
Figure 4.17. XRD texture spectrum for AlN film after 1600℃ 15 min annealing. (a)XRD spectra results. Pole figure for AlN film. (b) [0002] (c) [10$\bar{1}$1] (d) [10$\bar{1}$2] (e) [10$\bar{1}$3].

Referring to the XRD results of the as-deposited AlN film in Figure 4.17, the films are polycrystalline and primarily composed of 5 crystal orientations. The c-axis oriented [0002] orientation is predominant in the film, which meets the expectations based on the selected sputtering parameters. After the high-temperature annealing, the crystal orientation changed substantially. According to the Figure 5.1, except [0002] orientation, the diffraction intensity from the other orientations decreases significantly, especially for the [10$\bar{1}$1] orientation, which is almost absent after the annealing process.

5 Chapter 5: Photoluminescence, Cathodoluminescence and Raman Spectrum Results

5.1 PL results

Figure 5.1 depicts the room temperature photoluminescence spectrum of Ga-N co-doped 4H-SiC. The sample was excited with a 375nm laser, and the spectrum was deconvolved by using a Gaussian method. There are four peaks that were resolved, which are located at 410nm, 435nm, 530nm, and 630nm, respectively. The emission having wavelength centered at 435nm is identified as a recombination between Ga and N energy levels. According to the review in Chapter 2.5, the energy levels of Ga and N are 0.35eV above and 0.09 eV below, relevant to the valence and conduction band edges, respectively. Therefore, the energy difference between the donor and acceptor is 2.82eV or 440nm, which agrees with the peak location shown in the Figure 5.1. The wavelength difference may be attributed to the sub-energy level differences. In this sample, recombination between the Ga level and hexagonal site N is more favorable. The peak located at 530nm, having the highest intensity among the four peaks, is attributed to the single-level recombination at carbon vacancy defects. The 410nm peak can be assigned to the recombination between the Ga level and the conduction band. Since the AlN layer was preserved after annealing to passivate the surface, and as a semiconductor material, the defect levels in the AlN also have photon-emitting capabilities. The yellow emission around 630 nm is attributed to the absorption via aluminum vacancies, which were induced during the deposition process of the AlN film[59].

The spectra from the Ga-doped and un-doped regions were compared in Figure 5.1(b). The carbon vacancy defect emission around 530nm can be observed in both regions, which implies that the implantation does not significantly contribute to the carbon defects. The intensity of carbon defect recombination in different areas showing no obvious difference also supports this conclusion. The emission located around 435nm indicates a strong dependency on the Ga implantation since the emission cannot be observed in the undoped region. This proves that the emission does not relate to the AlN layer on the top. There is a slight peak shifting of the 530nm peak, which may be attributed to surface roughing during the implantation. Similarly, the 630nm Al vacancies emission also disappears outside the Ga-doped region. The distorted SiC crystal structure may encourage the formation of Al vacancies during the deposition process and thereby increase the vacancy density in the film. Since the Ga diffusion in the AlN layer can occur at a lower annealing temperature of 800℃, the formation of AlGaN may occur at the interface due to the AlN layer and Ga inter-diffusion[60]. As a semiconductor material, AlGaN has the potential to emit blue light, K. B. Nam et al. reported that AlGaN with 32 at% of Ga can emit light with 435nm wavelength [61]. However, based on the TEM-EDS results shown in Figure 6.1 (e), the Ga concentration is less than 5 at% in the AlN layer, which further proves that the emission at 435nm is not expected from the AlN capping layer.

5.2 CL results

The Figure 5.2 shows the CL spectrum results for the Ga-doped and undoped regions. Figure 5.2 (a) was deconvolved with the Gaussian method as well. The major DAP recombination emission peak has a wavelength of around 445nm. The peak located around 390nm is assigned to the 4H-SiC band-to-band recombination. Unlike PL spectral results, the Ga level to CB peak is not observed in the spectrum. The absence of the Ga-CB peak can be explained by the different excitation sources. In CL, the electrons are injected into the conduction band of the SiC. Therefore, instead of excitation and recombination between the donor and the acceptor levels, the electrons can migrate to the donor level and then recombine with holes in the acceptor level. Similar to the PL results, the 530nm emission is attributed to carbon vacancy defect recombination. Comparing Ga-doped and undoped spectra in Figure 5.2 (b), the emission intensity in the doped region is one order of magnitude stronger than the undoped region. Furthermore, the emission at 445nm is absent in the undoped region, which suggests that the 445nm emission is strongly correlated to the Ga implantation. Thereby, both PL and CL spectra lead to the conclusion that Ga-implanted 4H-SiC exhibits emission around 440nm via the donor-pair recombination mechanism.
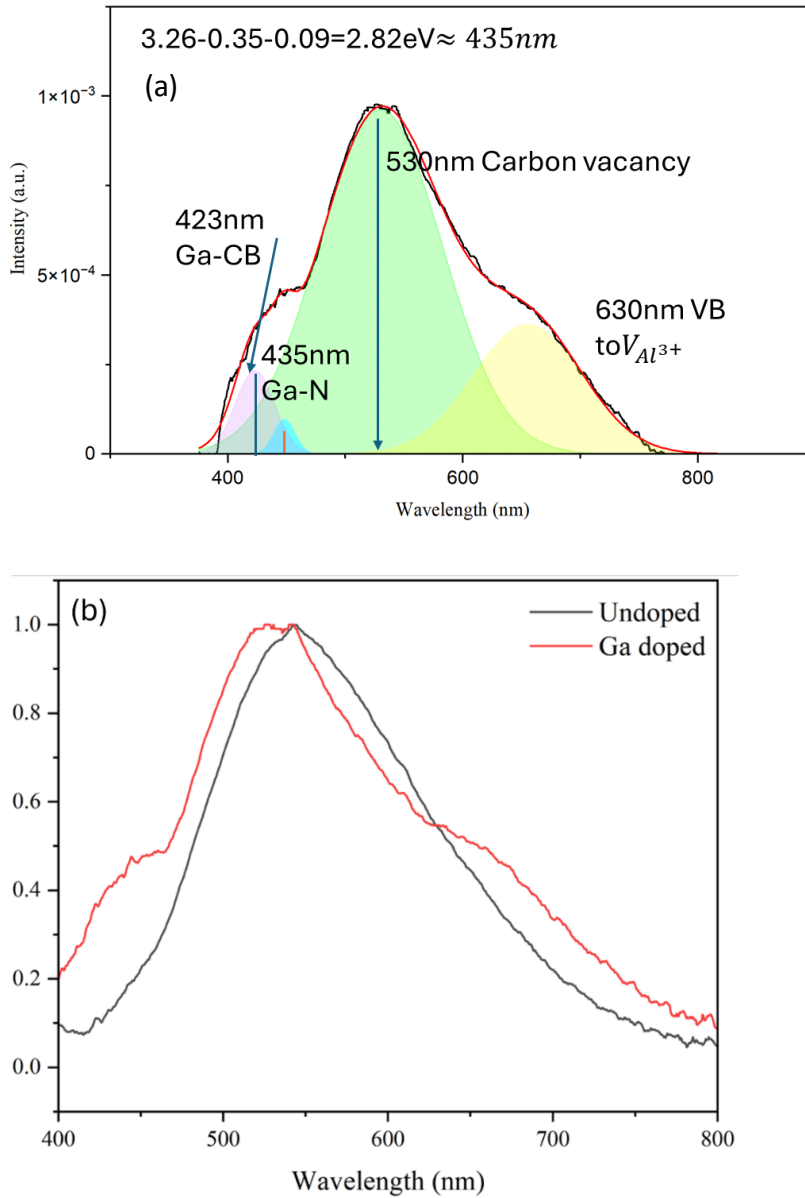
Figure 5.1. 1600℃ Annealed sample (a) Ga doped region deconvolved PL spectrum results (b) Comparison of the doped and undoped region.
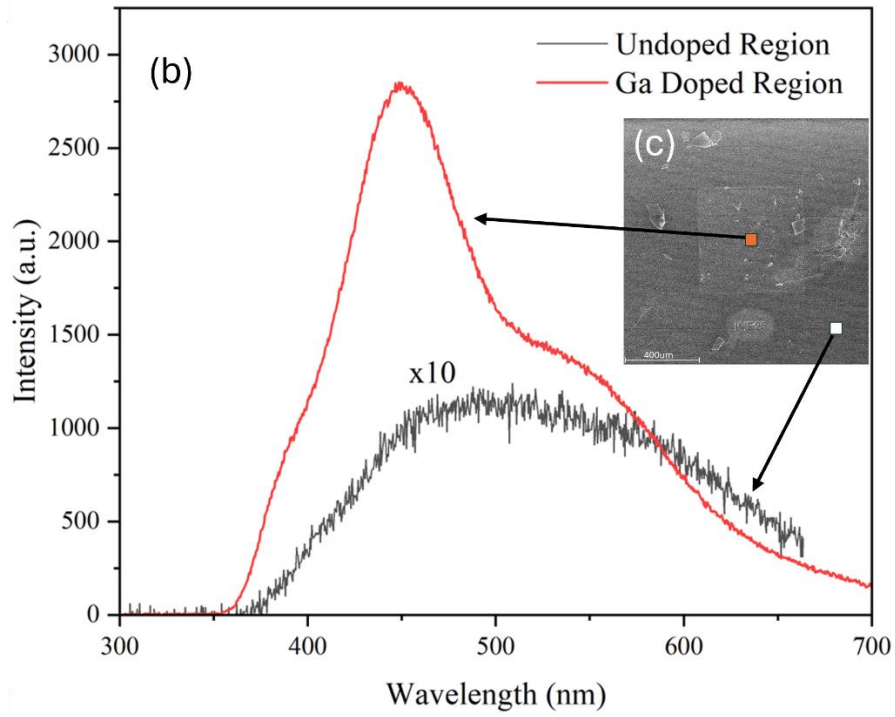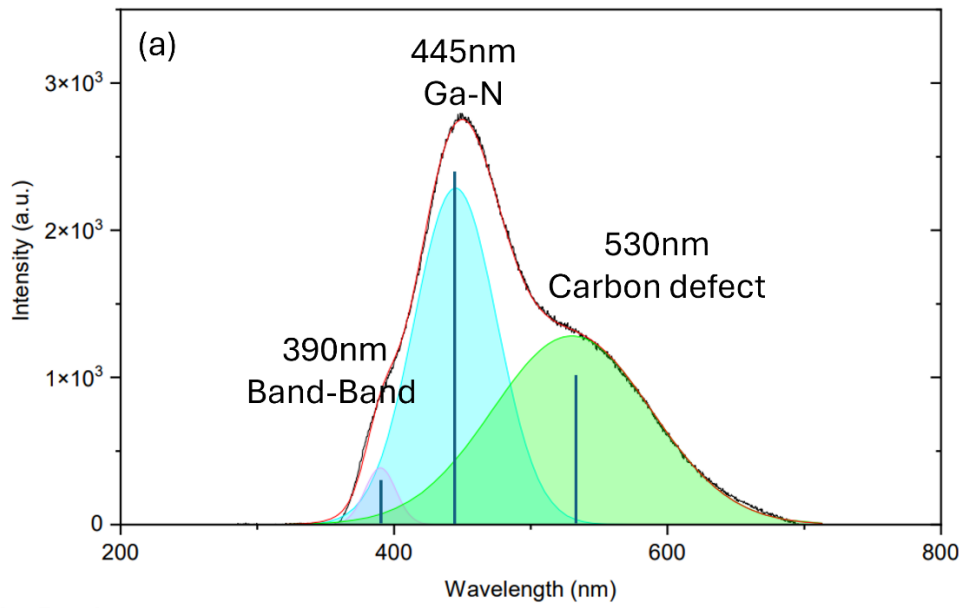
Figure 5.2. 1600℃ Annealed sample (a) Ga doped region deconvolved CL spectrum results (b) Comparison of the doped and undoped region (c) SEM image of CL spectrum sampling region, orange marker: doped region, white marker: undoped region.

5.3　Raman spectroscopy results
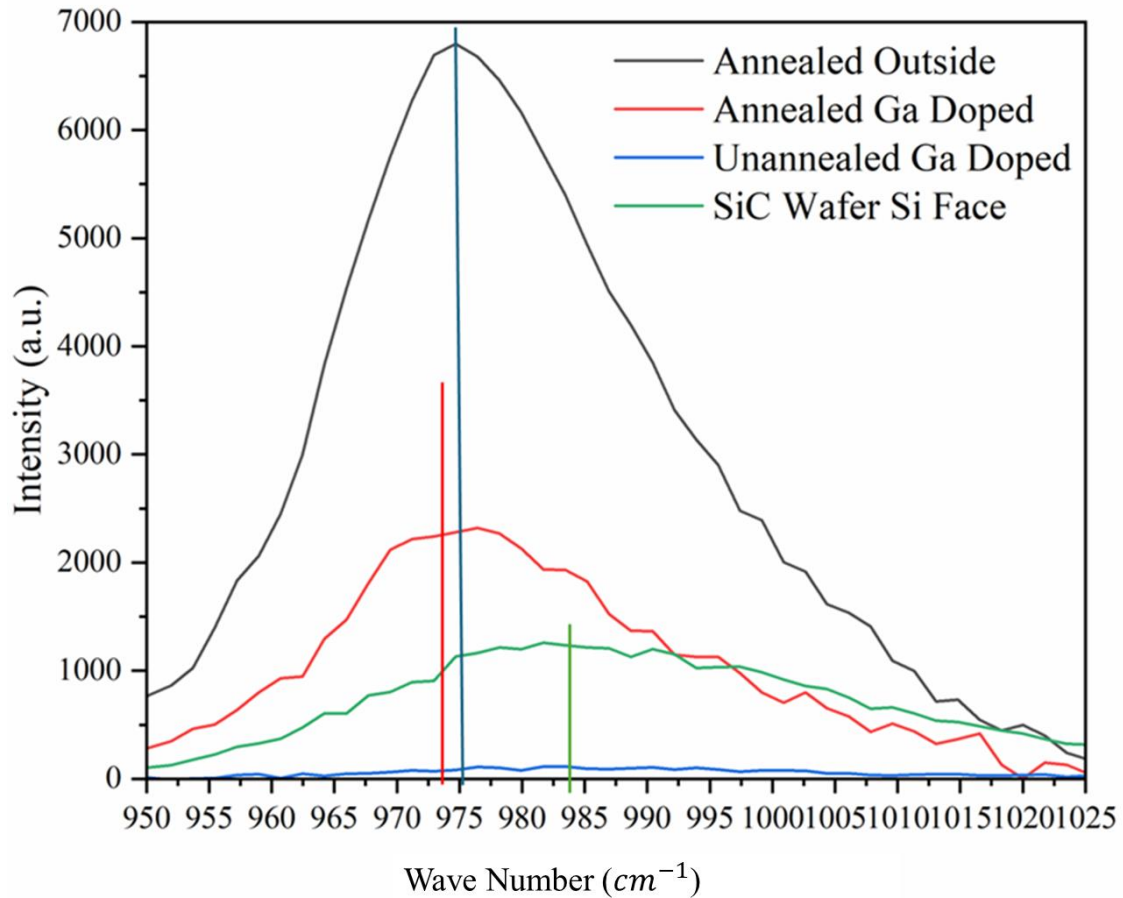
Figure 5.3. Comparison of Raman spectroscopy results of Ga doped and undoped region.

Raman spectroscopy was used to examine the doping and crystal recovery conditions in the as-implanted and annealed samples. In the SiC case, the longitudinal optical (LO) phonon mode is the focus, as the frequency and intensity of the LO mode are strongly

correlated with the free carrier concentration and crystallinity, respectively. Referring to the Raman results shown in Figure 5.3, the peak positions of SiC wafer, annealed undoped SiC, and annealed Ga doped SiC are located at $983\ cm^{-1}$, $976 cm^{-1}$ and $974 cm^{-1}$ respectively. Based on empirical values shown in Figure 3.4, the free carrier concentration are approximately equal to $8*10^{18}, 5*10^{18}\ and\ 3*10^{18} cm^{-3}$ respectively [54]. There is a deviation between the estimated and actual carrier concentration values, and the AlN layer may partially contribute to this difference. Since the absorption coefficient of 4H-SiC for a 532nm laser is relatively low, the Raman spectral results can be the superposition of the Ga implanted region and single crystalline substrate.

Although the empirical estimation deviates from the actual doping concentration value, especially for the SiC wafer sample, the trend of the frequency shift aligns with the PL and EDS results. The estimated free carrier concentration decrease indicates that p-type impurities experienced in-diffusion during the annealing. As the concentration of p-type impurities increases, compensation occurs between donors and acceptors levels that can effectively reduce the free carrier concentration in the crystal. The samples were annealed with an AlN capping layer, as shown in Figure 6.1 (d), and the in-diffused Al may unintentionally dope the SiC at the surface. The Ga-implanted region shows a lower wavenumber compared to the non-implanted region, which can be explained by larger amounts of p-type impurities that fit into the crystal. However, the amount of peak shift caused by Ga in-diffusion is significantly smaller than the peak shift caused by Al in-diffusion into SiC. The difference in shifting may be attributed to the atomic size difference

between the impurities, as smaller Al atoms have higher diffusion coefficients than Ga in SiC [62]. The LO mode peak was not observed in the as-implanted sample. To create a large Ga concentration gradient in the substrate and promote Ga in-diffusion, an excessive amount of Ga atoms was implanted into the substrate. The implantation induced not only substantial damage but also a Ga-segregated phase at the near-surface region. The damage and excessive Ga atoms likely disrupted the crystal vibrational mode in the substrate, resulting in the absence of the LO mode peak. After the annealing, the LO peak reappeared due to recrystallization and impurity redistribution, as shown in the TEM results in Figure 6.1(c) and Figure 6.2(c).

6 Chapter 6: TEM results
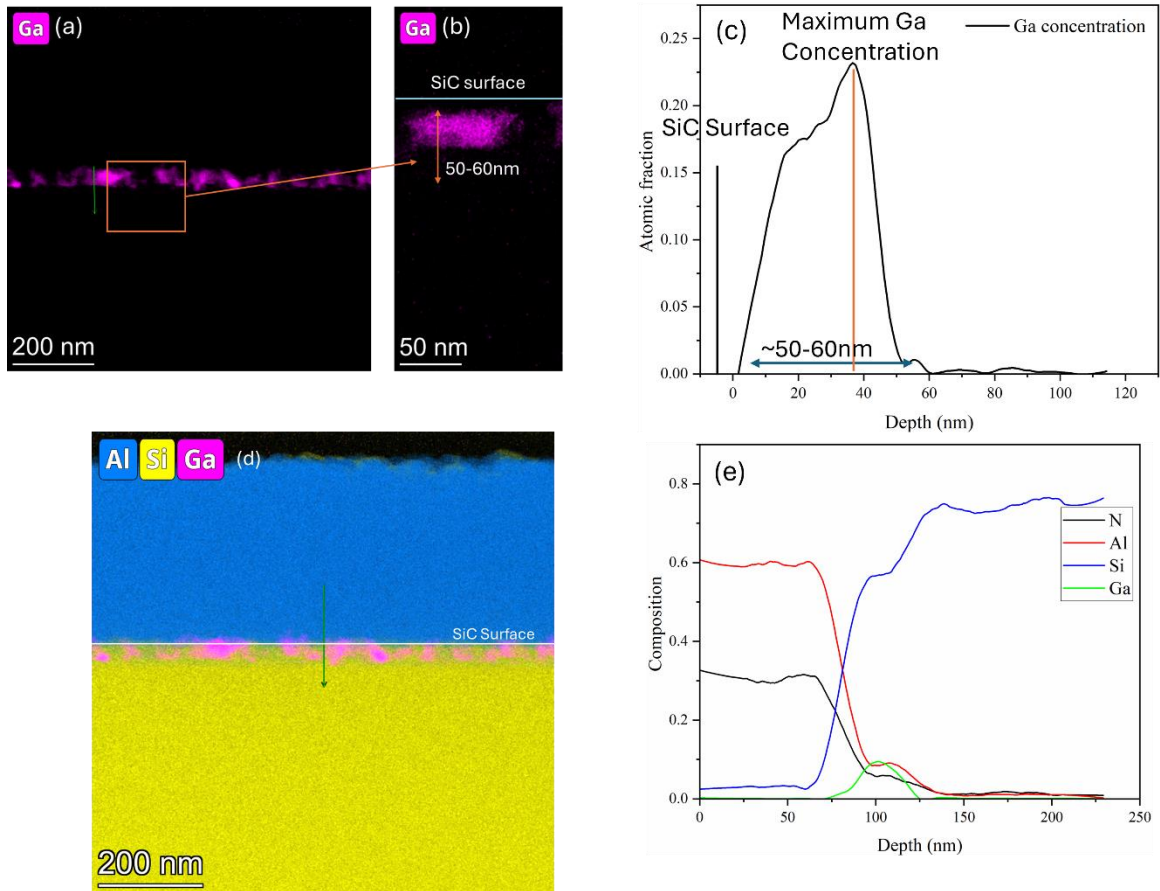
Figure 6.1. TEM EDS results of Sample annealed 15mins at 1600℃, (a) Mapping results, (b) Zoom-in of mapping results at the interface; (c) Line scan results of Ga concentration at near-surface region; (d) Mapping result of Al, Si, and Ga; (e) Line scan result of (d).

The TEM image of the sample cross-section EDS results are shown in Figure 6.1. According to the simulation results in Chapter 4.1, the depth with maximum Ga concentration is approximately 20nm from the surface, and the maximum projection depth is around 40nm. Based on Figure 6.1 (b), the Ga signal can be detected at a depth of 50-

60nm. These profile changes indicate that Ga atoms underwent in-diffusion during the annealing process, and the TEM-EDS results agree with the Raman spectroscopy results.
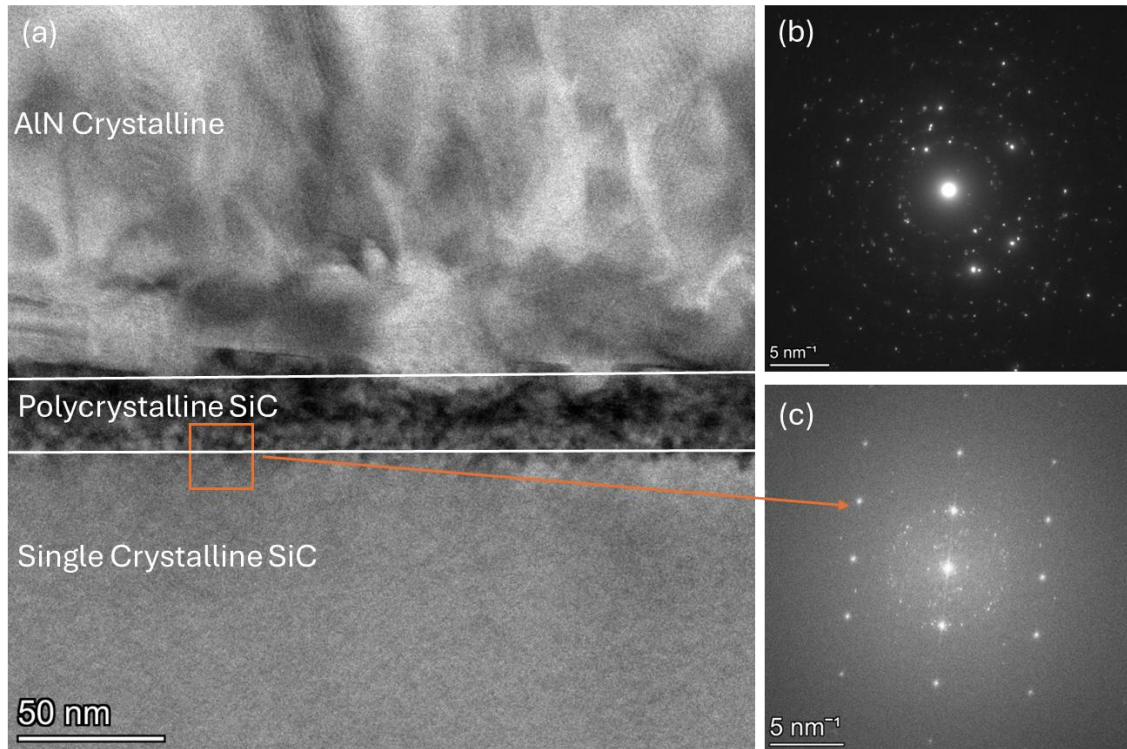
Figure 6.2. TEM Fast Fourier transfer (FFT) at the cross-section of Ga-doped 4H-SiC annealed at 1600°C for 15mins

As shown in Figure 6.2 (a), Georg Krugel et al. suggest that am amorphous AlN can form at the interface between the AlN layer and SiC substrate, the formation of the amorphous layer at the initial stage of the deposition is caused by a thin oxide layer on the surface. The oxide layer prevents the epitaxial growth of the AlN crystal on the SiC substrate. The electron beam diffraction results are shown in Figure 6.2 (c), display a ring pattern, indicating that the region with darker contrast has a polycrystalline structure.
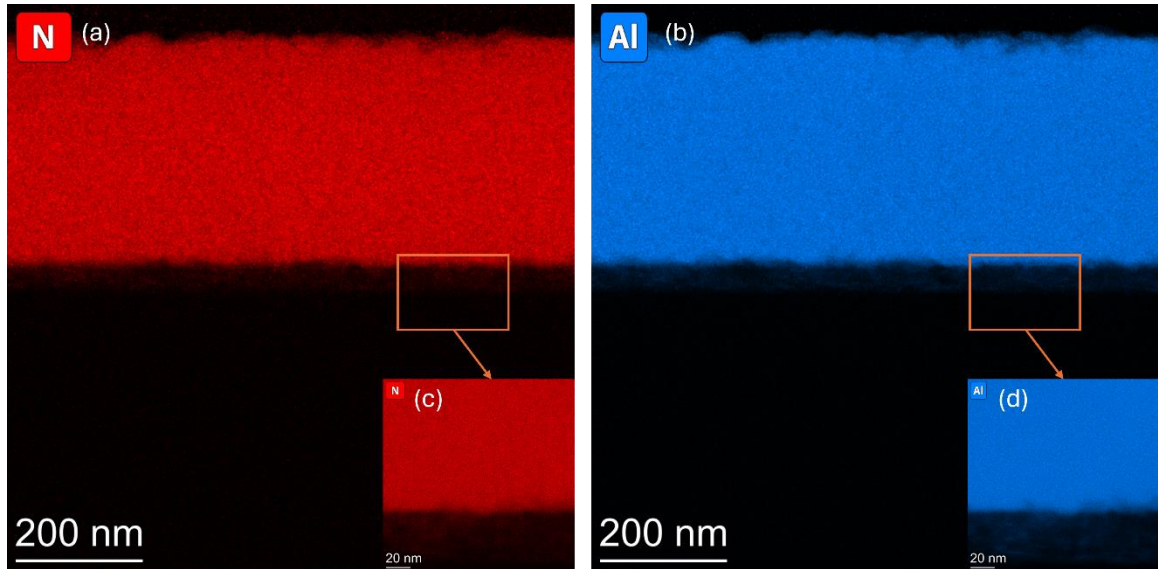
Figure 6.3. TEM-EDX mapping results of 1600℃ 15min annealed Ga doped sample. (a) N. (b) Al. (c) N mapping Zoom-in image at interface, weak N signal in SiC region (d) Al mapping Zoom-in image at interface weak Al signal in SiC region.

The Al and N TEM-EDS mapping is shown in Figure 6.3. In the zoomed-in image of Figure 6.3 (c) and (d), the Al and N can also be detected from the polycrystalline SiC region. The Al and N distribution regions in SiC are highly overlapped, which implies the same mechanism predominates the in-diffusion of the impurities. The ion implantation-induced damage may assist with the in-diffusion of impurities during the annealing through the defect-enhanced diffusion mechanism[63]. The crystal distortion induced by implantation promotes impurity diffusion and redistribution within the material. The redistribution of impurities in a lateral direction may extend several micrometers[64]. As mentioned in Chapter 2.5, Al is also a p-type dopant in SiC but has a lower ionization energy. This makes Al impurities easier to ionize compared to Ga. Therefore, the recombination involving the

Al level in the SiC bandgap may be suppressed by the presence of higher Ga energy levels [65].
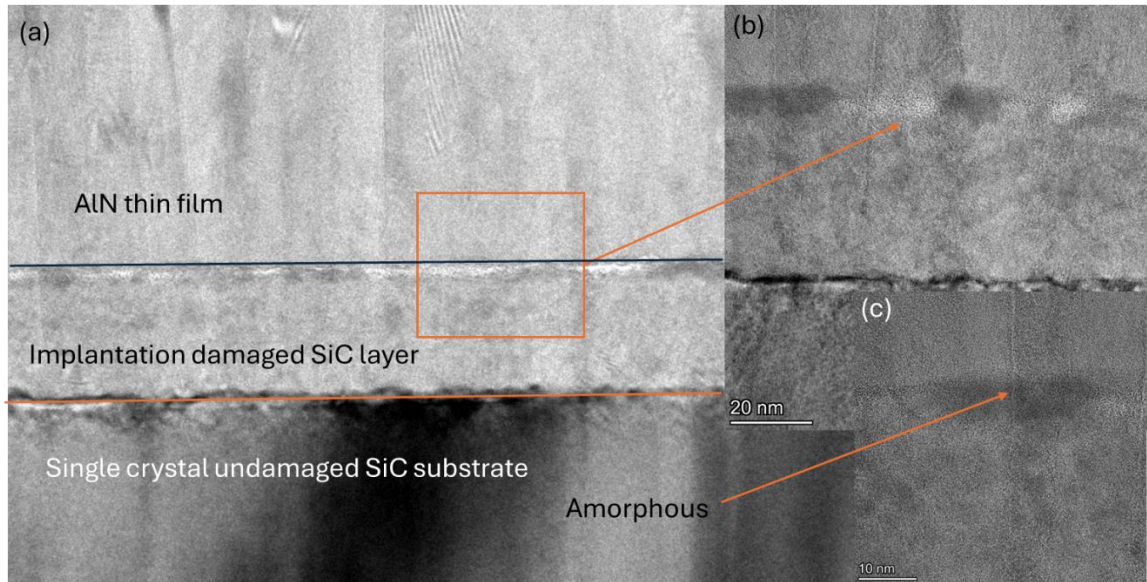
Figure 6.4. TEM cross-section results of Ga-implanted AlN-protected SiC annealed at 1000°C (a) Overall image (b) AlN-SiC interface (c) zoom-in image.

For the samples annealed at lower temperatures, the agglomeration of Ga can be found at the interface, as shown in Figure 6.4 (b-c) and Figure 6.5. The AlN layer acts as a barrier, which decreases the Ga out-diffusion tendency. As shown in the image, Ga is mainly distributed in the polycrystalline SiC layer and at the interface, which presents a different morphology and contrast compared to the SiC substrate in Figure 6.4 (a).
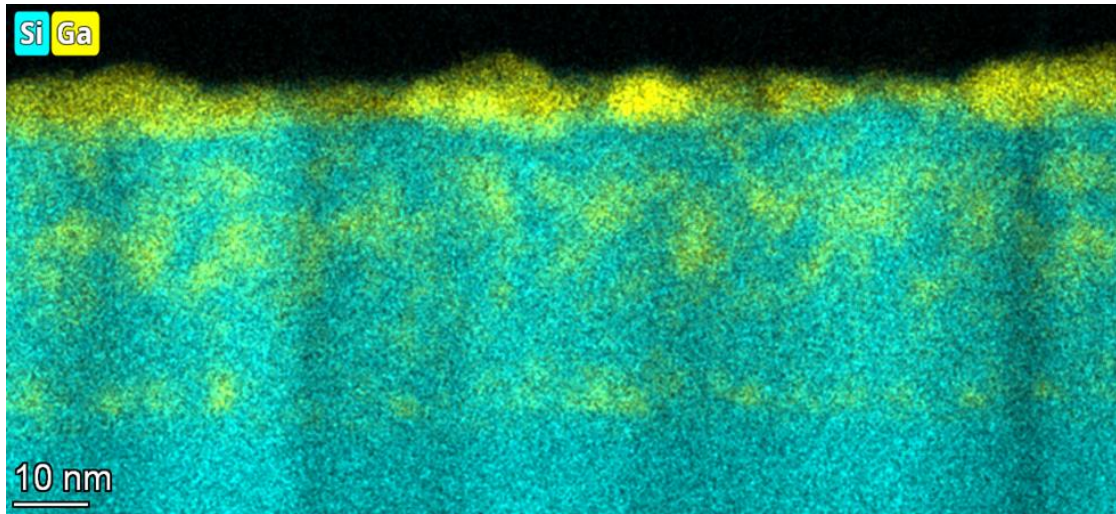
Figure 6.5. TEM cross-section Si and Ga EDS mapping results of Ga implanted SiC annealed at 1000℃.
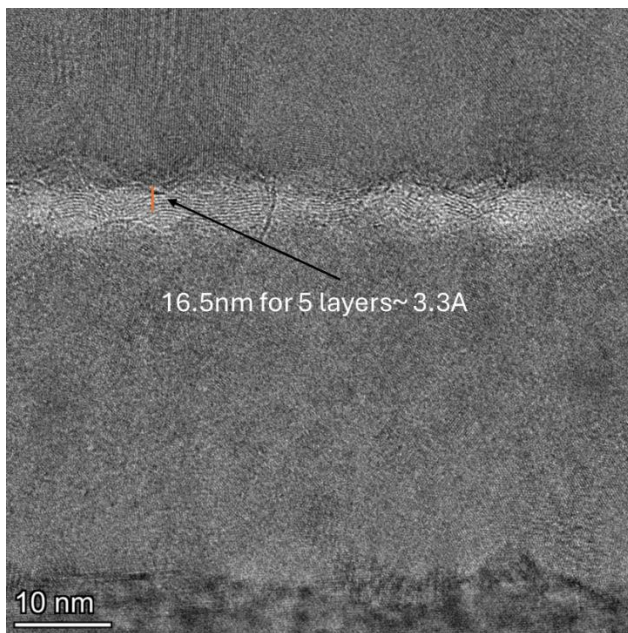
Figure 6.6. TEM cross-section results of Ga implanted, AlN protected SiC annealed at 1400℃.

As shown in Figure 6.6, a graphene structure can be observed in the sample annealed at 1400°C. The lattice spacing is approximately equal to 3.3Å which agrees with the reported value of 3.29 ± 0.13Å [66]. The formation of graphene at the interface of AlN/SiC is attributed to Si evaporation at high temperatures, leaving carbon atoms behind[66]. The formation of graphene has been observed during intercalation of foreign atomic layers at graphene/SiC interfaces at elevated temperatures[67-69]. However, due to the resolution limitations of our TEM image, the atomic layers spacings cannot be precisely calculated. Therefore, the existence of intercalation conditions remains unknown.
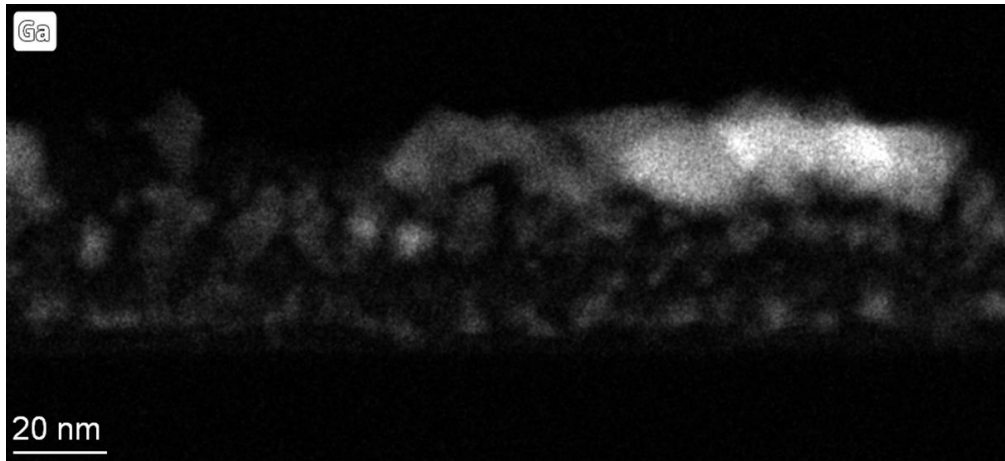
Figure 6.7. TEM-EDS 1400 annealed sample.

By comparing TEM-EDS mapping results among the samples annealed with different temperatures in Figure 6.1(a), Figure 6.5, and Figure 6.7. it is evident that the implanted Ga atoms tend to agglomerate and form amorphous precipitates after the annealing process. The precipitates tend to grow larger as the annealing temperature increases. The Ga-rich precipitates can act as nucleation centers for recrystallization during the annealing, which

may intensify Ga segregation due to random nucleation and growth. These Ga-rich precipitates may recrystallize at higher annealing temperatures[41].

7 Conclusion

In this thesis, Ga atoms were implanted into 4H-SiC wafers at an ultra-shallow depth. The sputtering deposition of AlN thin films was investigated in detail, and the orientation and morphology of the films were analyzed with the assistance of XRD and SEM. A set of optimized sputtering parameters was carried out to deposit a highly c-axis oriented AlN thin film on the SiC substrate. TEM-EDS and SIMS results demonstrated that the AlN encapsulation layer not only successfully mitigated surface erosion and Ga out-diffusion but also provided an additional source of nitrogen donors, effectively increasing the Fermi level and enhancing DAP recombination intensity.

The Ga-N co-doped SiC exhibited a spectral peak around 435nm wavelength, which was observed and analyzed using PL and CL techniques. In conclusion, the ion-implantation method has been proven to be an effective approach to achieving Ga-N DAP luminescence in 4H-SiC with high spatial resolution. Furthermore, this research presents the potential for developing SiC-based, high-performance down-conversion phosphors, which could be coupled with conventional nitride-based LEDs to enable white light emission.

8 Future works

In this project, only one Ga implantation concentration was selected as a trial to confirm that Ga-N donor-acceptor pair recombination emission in 4H-SiC is achievable. Future studies could focus on tuning the Ga concentration in SiC to achieve the optimal Ga-N concentration ratio for the most intensive emissions. Measurement of the absorption spectrum is a powerful tool for energy level analysis and could be included in future work to better understand the excitation and recombination mechanisms of energy levels. Raman spectroscopy results can be further analyzed and calibrated with empirical equations to establish the relationship between free carrier concentration and LO mode frequency in AlN-coated samples. As shown in the PL and CL results in Sections 5.1 and 5.2, the carbon-related defects dominate in the SiC, and the 530nm emission peak exhibits the most intense luminescence compared to other recombination mechanisms. The annealing parameters are worth further study and refinement to minimize the carbon vacancy density in the samples.

Additionally, the Ga-doped SiC has the potential to act as a down-conversion phosphor when coupled with a nitride p-n junction to emit white light. The configuration of such devices and manufacturing methods depicted in Figure 8.1 could be valuable research topics for future exploration.
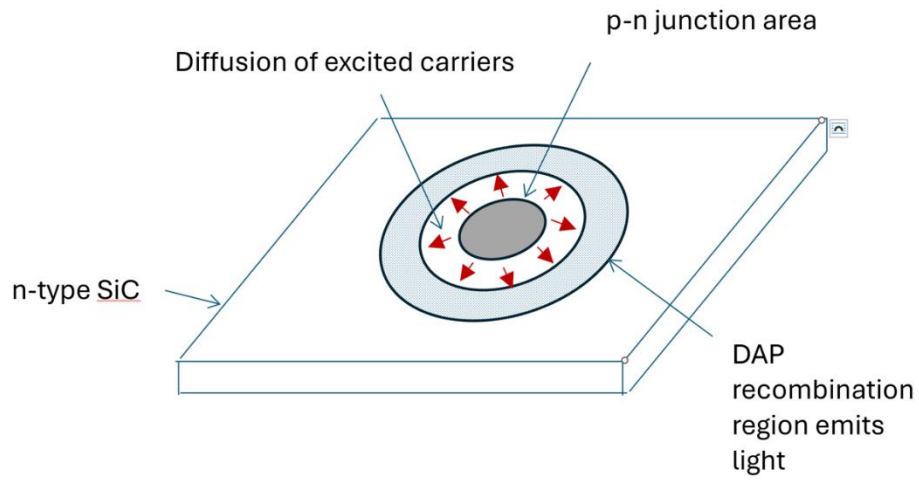
Figure 8.1. Schematic diagram of DAP down conversion phosphor coupled with nitride-based p-n junction. Carrier injected by p-n junction; the carriers diffuse toward surrounding phosphor material due to carrier concentrations difference. Carriers recombine and emit white light in the phosphor region.

9   Reference

[1]   P. J. Wellmann, "Review of SiC crystal growth technology," *Semiconductor Science and Technology,* vol. 33, no. 10, Oct 2018, Art no. 103001, doi: 10.1088/1361-6641/aad831.

[2]   N. G. Wright and A. B. Horsfall, "SiC sensors: a review," *Journal of Physics D-Applied Physics,* vol. 40, no. 20, pp. 6345-6354, Oct 2007, doi: 10.1088/0022-3727/40/20/s17.

[3]   L. B. Han, L. Liang, Y. Kang, and Y. F. Qiu, "A Review of SiC IGBT: Models, Fabrications, Characteristics, and Applications," *Ieee Transactions on Power Electronics,* vol. 36, no. 2, pp. 2080-2093, Feb 2021, doi: 10.1109/tpel.2020.3005940.

[4]   T. Kimoto, "Material science and device physics in SiC technology for high-voltage power devices," *Japanese Journal of Applied Physics,* vol. 54, no. 4, Apr 2015, Art no. 040103, doi: 10.7567/jjap.54.040103.

[5]   F. Fuchs *et al.*, "Silicon carbide light-emitting diode as a prospective room temperature source for single photons," *Scientific Reports,* vol. 3, Apr 2013, Art no. 1637, doi: 10.1038/srep01637.

[6]   S. S. Lin, "Light-Emitting Two-Dimensional Ultrathin Silicon Carbide," *Journal of Physical Chemistry C,* vol. 116, no. 6, pp. 3951-3955, Feb 2012, doi: 10.1021/jp210536m.

[7]   W. A. Nevin, H. Yamagishi, M. Yamaguchi, and Y. Tawada, "EMISSION OF BLUE-LIGHT FROM HYDROGENATED AMORPHOUS-SILICON CARBIDE," *Nature,* vol. 368, no. 6471, pp. 529-531, Apr 1994, doi: 10.1038/368529a0.

[8]   T. Kimoto and J. A. Cooper, "Fundamentals of Silicon Carbide Technology: Growth, Characterization, Devices, and Applications," Fundamentals of Silicon Carbide Technology: Growth, Characterization, Devices, and Applications, 978-1-118-31353-4; 978-1-118-31352-7, 2014. [Online]. Available: <Go to ISI>://WOS:000359940300017

[9]   G. Rescher. "Behavior of sic-mosfets under temperature and voltage stress." reposiTUm. https://repositum.tuwien.at/handle/20.500.12708/7336 (accessed Nov. 13, 2024).

[10]   D. F. Holcomb, "KITTEL,C - INTRODUCTION TO SOLID STATE PHYSICS," *American Journal of Physics,* vol. 35, no. 6, pp. 547-&, 1967. [Online]. Available: <Go to ISI>://WOS:A19679620400028.

[11]   G. Krugel, F. Jenkner, A. Moldovan, W. Wolke, J. Rentsch, and R. Preu, "Investigations on the passivation mechanism of AlN:H and AlN:H-SiN:H stacks," in *4th International Conference on Crystalline Silicon Photovoltaics (SiliconPV)*, ECN, Hertogenbosch, NETHERLANDS, Mar 24-27 2014, vol. 55, in Energy Procedia, 2014, pp. 797-804, doi: 10.1016/j.egypro.2014.08.062. [Online]. Available: <Go to ISI>://WOS:000346095800111

[12]   A. Naugarhiya, P. Wakhradkar, P. N. Kondekar, G. C. Patil, and R. M. Patrikar, "Analytical model for 4H-SiC superjunction drift layer with anisotropic properties for ultrahigh-voltage applications," *Journal of Computational Electronics,* vol. 16, no. 1, pp. 190-201, Mar 2017, doi: 10.1007/s10825-016-0942-y.

[13]   P. G. Neudeck, "Silicon Carbide Technology," 2006.

[14]   F. Bechstedt, "Polytypism and Properties of Silicon Carbide," *physica status solidi (b),*   vol.   202,   1997,   doi: https://doi.org/10.1002/1521-3951(199707)202:1<35::AID-PSSB35>3.0.CO;2-8.

[15]   S. C. R. F. Davis, *"* Reference Module in Materials Science and Materials Engineering, 2017. doi:10.1016/b978-0-12-803581-8.02445-0 "Silicon Carbide," *Reference Module in Materials Science and Materials Engineering,* 2017, doi: 10.1016/b978-0-12-803581-8.02445-0.

[16]   S. Kamiyama *et al.*, "Extremely high quantum efficiency of donor-acceptor-pair emission in N-and-B-doped 6<i>H</i>-SiC," *Journal of Applied Physics,* vol. 99, no. 9, May 2006, Art no. 093108, doi: 10.1063/1.2195883.

[17]   S. K. Lilov, "THERMODYNAMIC ANALYSIS OF THE GAS-PHASE AT THE DISSOCIATIVE EVAPORATION OF SILICON-CARBIDE," *Crystal Research and Technology,* vol. 28, no. 4, pp. 503-510, 1993, doi: 10.1002/crat.2170280416.

[18]   D. D. Avrov, A. S. Bakin, S. I. Dorozhkin, V. P. Rastegaev, and Y. M. Tairov, "The analysis of mass transfer in system β-SiC-α-SiC under silicon carbide sublimation growth," *Journal of Crystal Growth,* vol. 198, pp. 1011-1014, Mar 1999, doi: 10.1016/s0022-0248(98)01215-9.

[19]   Y. M. Tairov, N. S. Peev, N. A. Smirnova, and A. A. Kalnin, "LIQUID-PHASE EPITAXY OF SIC IN THE SYSTEM SI-TB-SIC BY TEMPERATURE-GRADIENT ZONE-MELTING (I) - INVESTIGATION OF SOLUBILITIES IN THE SYSTEM SI-TB-SIC," *Crystal Research and Technology,* vol. 21, no. 12, pp. 1503-1507, 1986, doi: 10.1002/crat.2170211203.

[20]   F. K. Yam and Z. Hassan, "Innovative advances in LED technology," *Microelectronics Journal,* vol. 36, no. 2, pp. 129-137, Feb 2005, doi: 10.1016/j.mejo.2004.11.008.

[21]   N. Zheludev, "The life and times of the LED - a 100-year history," *Nature Photonics,* vol. 1, no. 4, pp. 189-192, Apr 2007, doi: 10.1038/nphoton.2007.34.

[22]   Y. J. Wang, J. M. Alonso, and X. B. Ruan, "A Review of LED Drivers and Related Technologies," *Ieee Transactions on Industrial Electronics,* vol. 64, no. 7, pp. 5754-5765, Jul 2017, doi: 10.1109/tie.2017.2677335.

[23]   P. Mottier, *LED for Lighting Applications*. John Wiley & Sons, 2010.

[24]   I. Akasaki, "Key inventions in the history of nitride-based blue LED and LD," *Journal of Crystal Growth,* vol. 300, no. 1, pp. 2-10, Mar 2007, doi: 10.1016/j.jcrysgro.2006.10.259.

[25]   B. Sun, X. P. Jiang, K. C. Yung, J. J. Fan, and M. G. Pecht, "A Review of Prognostic Techniques for High-Power White LEDs," *Ieee Transactions on Power Electronics,* vol. 32, no. 8, pp. 6338-6362, Aug 2017, doi: 10.1109/tpel.2016.2618422.

[26]   J. Cho, J. H. Park, J. K. Kim, and E. F. Schubert, "White light-emitting diodes: History, progress, and future," *Laser & Photonics Reviews,* vol. 11, no. 2, Mar 2017, Art no. 1600147, doi: 10.1002/lpor.201600147.

[27]   J. Edmond, H. Kong, A. Suvorov, D. Waltz, and C. Carter, "6H-Silicon carbide light emitting diodes and UV photodiodes," *Physica Status Solidi a-Applied Research,* vol. 162, no. 1, pp. 481-491, Jul 1997, doi: 10.1002/1521-396x(199707)162:1<481::Aid-pssa481>3.0.Co;2-o.

[28]   J. Edmond *et al.*, "High efficiency GaN-based LEDs and lasers on SiC," *Journal of Crystal Growth,* vol. 272, no. 1-4, pp. 242-250, Dec 2004, doi: 10.1016/j.jcrysgro.2004.08.056.

[29]   H. S. Kong, J. Ibbetson, and J. Edmond, "Status of GaN/SiC-based LEDs and their application in solid state lighting," in *10th International Conference on Nitride Semiconductors (ICNS)*, Washington, DC, Aug 25-30 2013, vol. 11, in Physica Status Solidi C-Current Topics in Solid State Physics, 2014, pp. 621-623, doi: 10.1002/pssc.201300458. [Online]. Available: <Go to ISI>://WOS:000346071300062

[30]   M. A. L. Johnson *et al.*, "MBE growth and properties of GaN and AlxGa1-xN on GaN/SiC substrates," *Journal of Electronic Materials,* vol. 25, no. 5, pp. 793-797, May 1996, doi: 10.1007/bf02666638.

[31]   A. Kitai, "Principles of Solar Cells, LEDs and Diodes The role of the PN junction Introduction," Principles of Solar Cells, Leds and Diodes: The Role of the Pn Junction, 978-1-119-97455-0; 978-1-4443-1834-0, 2011. [Online]. Available: <Go to ISI>://WOS:000337045700001

[32]   M. G. X.-D. DANG, and T.-Q. NGUYEN, "Organic solar cell materials and devices characterized by conductive and photoconductive atomic force microscopy," *World Scientific Series in Nanoscience and Nanotechnology,* vol. pp. 73–113,, Mar. 2013, doi: 10.1142/9789814434713_0003.

[33]   R. H. a. M. S. O'Sullivan, *Fiber Optic Measurement Techniques*. Amsterdam: Elsevier/Academic Press, 2009.

[34]   O. Z. Sharaf and M. E. Orhan, "Concentrated photovoltaic thermal (CPVT) solar collector systems: Part I - Fundamentals, design considerations and current technologies," *Renewable & Sustainable Energy Reviews,* vol. 50, pp. 1500-1565, Oct 2015, doi: 10.1016/j.rser.2015.05.036.

[35]   J. I. Pankove, *OPTICAL PROCESSES IN SEMICONDUCTORS*. New York: Dover Publication, Inc., 1971.

[36]   A. Yang, K. Murata, T. Miyazawa, T. Tawara, and H. Tsuchida, "Time-resolved photoluminescence spectral analysis of phonon-assisted DAP and e-A recombination in N plus B-doped <i>n-</i>type 4H-SiC epilayers," *Journal of Physics D-Applied Physics,* vol. 52, no. 10, Mar 2019, Art no. 1olt01, doi: 10.1088/1361-6463/aaf8e9.

[37]   Y. C. Huang, R. Wang, D. R. Yang, and X. D. Pi, "Impurities in 4H silicon carbide: Site preference, lattice distortion, solubility, and charge transition levels," *Journal of Applied Physics,* vol. 135, no. 19, May 2024, Art no. 195703, doi: 10.1063/5.0190242.

[38]   Y. Negoro, K. Katsumoto, T. Kimoto, and H. Matsunami, "Electronic behaviors of high-dose phosphorus-ion implanted 4H-SiC(0001)," *Journal of Applied Physics,* vol. 96, no. 1, pp. 224-228, Jul 2004, doi: 10.1063/1.1756213.

[39]   M. Bockstedte, A. Mattausch, and O. Pankratov, "Solubility of nitrogen and phosphorus in 4H-SiC: A theoretical study," *Applied Physics Letters,* vol. 85, no. 1, pp. 58-60, Jul 2004, doi: 10.1063/1.1769075.

[40]   M. K. Linnarsson *et al.*, "Solubility limits of dopants in 4H-SiC," *Applied Surface Science,* vol. 203, pp. 427-432, Jan 2003, Art no. Pii s0169-4332(02)00694-3, doi: 10.1016/s0169-4332(02)00694-3.

[41]   G. Lim and A. Kar, "Effects of laser scans on the diffusion depth and diffusivity of gallium in n-type 4H-SiC during laser doping," *Materials Science and Engineering B-Advanced Functional Solid-State Materials,* vol. 176, no. 8, pp. 660-668, May 2011, doi: 10.1016/j.mseb.2011.02.011.

[42]   Y. A. Vodakov *et al.*, "SILICON-CARBIDE DOPED WITH GALLIUM," *Physica Status Solidi a-Applied Research,* vol. 35, no. 1, pp. 37-42, 1976, doi: 10.1002/pssa.2210350103.

[43]   G. Dearnaley, "ION-IMPLANTATION," *Nature,* vol. 256, no. 5520, pp. 701-705, 1975, doi: 10.1038/256701a0.

[44]   T. Seyller, "Passivation of hexagonal SiC surfaces by hydrogen termination," *Journal of Physics-Condensed Matter,* vol. 16, no. 17, pp. S1755-S1782, May 2004, Art no. Pii s0953-8984(04)65147-2, doi: 10.1088/0953-8984/16/17/016.

[45]   P. Grivickas, J. Linnros, and V. Grivickas, "Carrier diffusion characterization in epitaxial 4H-SiC," *Journal of Materials Research,* vol. 16, no. 2, pp. 524-528, Feb 2001, doi: 10.1557/jmr.2001.0075.

[46]   O. Kordina, J. P. Bergman, C. Hallin, and E. Janzen, "The minority carrier lifetime of n-type 4H- and 6H-SiC epitaxial layers," *Applied Physics Letters,* vol. 69, no. 5, pp. 679-681, Jul 1996, doi: 10.1063/1.117804.

[47]   N. T. Son, W. M. Chen, J. L. Lindström, B. Monemar, and E. Janzén, "Carbon-vacancy related defects in 4H-and 6H-SIC," *Materials Science and Engineering B-Solid State Materials for Advanced Technology,* vol. 61-2, pp. 202-206, Jul 1999, doi: 10.1016/s0921-5107(98)00502-9.

[48]   T. Kobayashi and Y. Matsushita, "Structure and energetics of carbon defects in SiC (0001)/SiO$_2$ systems at realistic temperatures: Defects in SiC, SiO$_2$, and at their interface," *Journal of Applied Physics,* vol. 126, no. 14, Oct 2019, Art no. 145302, doi: 10.1063/1.5100754.

[49]   T. Hiyoshi and T. Kimoto, "Elimination of the Major Deep Levels in n- and p-Type 4H-SiC by Two-Step Thermal Treatment," *Applied Physics Express,* vol. 2, no. 9, Sep 2009, Art no. 091101, doi: 10.1143/apex.2.091101.

[50]   Y. W. Yang, Z. Y. Tong, X. D. Pi, D. R. Yang, and Y. C. Huang, "Advances and challenges in 4H silicon carbide: defects and impurities," *Physica Scripta,* vol. 99, no. 9, Sep 2024, Art no. 092001, doi: 10.1088/1402-4896/ad6697.

[51]   W. Kern, *Overview and Evolution of Silicon Wafer Cleaning Technology* (Handbook of Silicon Wafer Cleaning Technology, 2nd Edition, no. 978-0-08-094746-4; 978-0-8155-1554-8). 2008, pp. 3-92.

[52]   W. Kern, *CITATION CLASSIC - CLEANING SOLUTIONS BASED ON HYDROGEN-PEROXIDE FOR USE IN SILICON SEMICONDUCTOR TECHNOLOGY* (Current Contents/Engineering Technology & Applied Sciences, no. 11). 1983, pp. 18-18.

[53]   M. Chafai *et al.*, "Raman scattering from LO phonon-plasmon coupled modes and Hall-effect in <i>n</i>-type silicon carbide 4H-SiC," *Journal of Applied Physics,* vol. 90, no. 10, pp. 5211-5215, Nov 2001, doi: 10.1063/1.1410884.

[54]   J. C. Burton *et al.*, "Spatial characterization of doped SiC wafers by Raman spectroscopy," in *2nd ECS Symposium on III-V Nitride Materials and Processes, at the 192nd Meeting of the Electrochemical-Society*, Paris, France, Aug 31-Sep 05 1997, vol. 97, in Electrochemical Society Series, 1998, pp. 220-227. [Online]. Available: <Go to ISI>://WOS:000072820400024. [Online]. Available: <Go to ISI>://WOS:000072820400024

[55]   Y. Zhang, W. J. Weber, W. Jiang, C. M. Wang, V. Shutthanandan, and A. Hallén, "Effects of implantation temperature on damage accumulation in Al-implanted 4H-SiC," *Journal of Applied Physics,* vol. 95, no. 8, pp. 4012-4018, Apr 2004, doi: 10.1063/1.1666974.

[56]   X. Q. Jiao, Y. Shi, H. Zhong, R. Zhang, and J. Yang, "AlN thin films deposited on different Si-based substrates through RF magnetron sputtering," *Journal of Materials Science-Materials in Electronics,* vol. 26, no. 2, pp. 801-808, Feb 2015, doi: 10.1007/s10854-014-2467-0.

[57]   B. H. Hwang, C. S. Chen, H. Y. Lu, and T. C. Hsu, "Growth mechanism of reactively sputtered aluminum nitride thin films," *Materials Science and Engineering a-Structural Materials Properties Microstructure and Processing,* vol. 325, no. 1-2, pp. 380-388, Feb 2002, Art no. Pii s093(01)01477-0, doi: 10.1016/s0921-5093(01)01477-0.

[58]   X. P. Kuang *et al.*, "AlN films prepared on 6H-SiC substrates under various sputtering pressures by RF reactive magnetron sputtering," *Applied Surface Science,* vol. 263, pp. 62-68, Dec 2012, doi: 10.1016/j.apsusc.2012.08.121.

[59]   A. Sedhain, L. Du, J. H. Edgar, J. Y. Lin, and H. X. Jiang, "The origin of 2.78 eV emission and yellow coloration in bulk AlN substrates," *Applied Physics Letters,* vol. 95, no. 26, Dec 2009, Art no. 262104, doi: 10.1063/1.3276567.

[60]   M. Nemoz *et al.*, "Interdiffusion of Al and Ga in AlN/AlGaN superlattices grown by ammonia-assisted molecular beam epitaxy," *Superlattices and Microstructures,* vol. 150, Feb 2021, Art no. 106801, doi: 10.1016/j.spmi.2020.106801.

[61]   K. B. Nam, M. L. Nakarmi, J. Y. Lin, and H. X. Jiang, "Deep impurity transitions involving cation vacancies and complexes in AlGaN alloys," *Applied Physics Letters,* vol. 86, no. 22, May 2005, Art no. 222108, doi: 10.1063/1.1943489.

[62]   E. N. Mokhov, "Doping of sic crystals during sublimation growth and diffusion," *Crystal Growth,* Nov. 2019, doi: 10.5772/intechopen.82346.

[63]   B. Gerard, G. Pijaudier-Cabot, and C. Laborderie, "Coupled diffusion-damage modelling and the implications on failure due to strain localisation," *International Journal of Solids and Structures,* vol. 35, no. 31-32, pp. 4107-4120, Nov 1998, doi: 10.1016/s0020-7683(97)00304-1.

[64]   J. Müting *et al.*, "Spatially Resolved Diffusion of Aluminum in 4H-SiC During Postimplantation Annealing," *Ieee Transactions on Electron Devices,* vol. 67, no. 10, pp. 4360-4365, Oct 2020, doi: 10.1109/ted.2020.3018690.

[65]   X. Liu, S. Y. Zhuo, P. Gao, W. Huang, C. F. Yan, and E. W. Shi, "Donor-acceptor-pair emission in fluorescent 4H-SiC grown by PVT method," *Aip Advances,* vol. 5, no. 4, Apr 2015, Art no. 047133, doi: 10.1063/1.4919012.

[66]   A. Kakanakova-Georgieva *et al.*, "Nanoscale phenomena ruling deposition and intercalation of AlN at the graphene/SiC interface," *Nanoscale,* vol. 12, no. 37, pp. 19470-19476, Oct 2020, doi: 10.1039/d0nr04464d.

[67]   H. El-Sherif *et al.*, "Scalable Characterization of 2D Gallium-Intercalated Epitaxial Graphene," *Acs Applied Materials & Interfaces,* vol. 13, no. 46, pp. 55428-55439, Nov 2021, doi: 10.1021/acsami.1c14091.

[68]   N. Feldberg *et al.*, "Spontaneous intercalation of Ga and In bilayers during plasma-assisted molecular beam epitaxy growth of GaN on graphene on SiC," *Nanotechnology,* vol. 30, no. 37, Sep 2019, Art no. 375602, doi: 10.1088/1361-6528/ab261f.

[69]   F. Niefind *et al.*, "Watching (De)Intercalation of 2D Metals in Epitaxial Graphene: Insight into the Role of Defects," *Small,* vol. 20, no. 11, Mar 2024, doi: 10.1002/smll.202306554.